

Source geometry estimation using the mass excess criterion to constrain 3-D radial inversion of gravity data

Vanderlei C. Oliveira, Jr,¹ Valéria C. F. Barbosa¹ and João B. C. Silva²

¹Observatório Nacional, Gal. José Cristino, 77, São Cristóvão, Rio de Janeiro, 20921-400, Brazil. E-mail: vandscoelho@gmail.com

²Universidade Federal do Pará, Dep. Geofísica CG, Caixa Postal 1611, 66017-900, Belém, Pará, Brazil

Accepted 2011 July 26. Received 2011 July 26; in original form 2010 October 13

SUMMARY

We present a gravity-inversion method for estimating the geometry of an isolated 3-D source, assuming prior knowledge about its top and density contrast. The subsurface region containing the geological sources is discretized into an ensemble of 3-D vertical prisms juxtaposed in the vertical direction of a right-handed coordinate system. The prisms' thicknesses and density contrasts are known, but their horizontal cross-sections are described by unknown polygons. The horizontal coordinates of the polygon vertices approximately represent the edges of horizontal depth slices of the 3-D geological source. The polygon vertices of each prism are described by polar coordinates with an unknown origin within the prism. Our method estimates the horizontal Cartesian coordinates of the unknown origin and the radii associated with the vertices of each polygon for a fixed number of equally spaced central angles from 0° to 360°. By estimating these parameters from gravity data, we retrieve a set of vertically stacked prisms with polygonal horizontal sections that represents a set of juxtaposed horizontal depth slices of the estimated source. This set, therefore, approximates the 3-D source's geometry. To obtain stable estimates we impose constraints on the source shape. The judicious use of first-order Tikhonov regularization on either all or a few parameters allows estimating both vertical and inclined sources whose shapes can be isometric or anisometric. The estimated solution, despite being stable and fitting the data, will depend on the maximum depth assumed for the set of juxtaposed 3-D prisms. To reduce the class of possible solutions compatible with the gravity anomaly and the constraints, we use a criterion based on the relationship between the data-misfit measure and the estimated total-anomalous mass computed along successive inversions, using different tentative maximum depths for the set of assumed juxtaposed 3-D prisms. In applying this criterion, we plotted the curve of the estimated total-anomalous mass m_t versus data-misfit measure s for the range of different tentative maximum depths. The tentative value for the maximum depth producing the smallest value of data-misfit measure in the $m_t \times s$ curve is the best estimate of the true (or minimum) depth to the bottom of the source, depending on whether the true source produces a gravity anomaly that is able (or not) to resolve the depth to the source bottom. This criterion was theoretically deduced from Gauss' theorem. Tests with synthetic data shows that the correct depth-to-bottom estimate of the source is obtained if the minimum of s on the $m_t \times s$ curve is well defined; otherwise this criterion provides just a lower bound estimate of the source's depth to the bottom. These synthetic results show that the method efficiently recovers source geometries dipping at different angles. Test on real data from the Matsitama intrusive complex (Botswana) retrieved a dipping intrusion with variable dips and strikes and with bottom depth of 8.0 ± 0.5 km.

Key words: Numerical solutions; Inverse theory; Gravity anomalies and Earth structure.

1 INTRODUCTION

The reconstruction of 3-D (or 2-D) geological sources from a discrete set of gravity data measured at the Earth's surface usually follows two strategies. The first one is the interactive gravity forward

modelling and the second strategy comprises the gravity-inversion methods.

The interactive gravity forward modelling consists in inferring a representation of the 3-D (or 2-D) geometry of geological sources in the subsurface that fits the observed gravity data. Hence, the

interactive gravity forward modelling requires the specification of tentative source geometry and it allows the interactivity and flexibility of introducing geological information about the study area at the interpreter's discretion. Therefore, the interpreter's conception about the geology of the study area is incorporated in a direct way. However, this task involves an exhaustive, tedious and time-consuming trial-and-error procedure wherein the interpreter must supervise both the data fit and the construction of geologically meaningful sources. Most recently substantial effort has been devoted towards making the 3-D (or 2-D) interactive gravity forward modelling more attractive and operational. For example, Silva & Barbosa (2006) and Silva Dias *et al.* (2009), respectively, assuming 2-D and 3-D sources, combined the best features of interactive forward modelling (the interactivity and flexibility of introducing geological information) and of automatic inversion (the facility of automatically fitting the observations). These authors' approaches are similar to a standard interactive gravity forward modelling but differ from it in automatically fitting the observations and in requiring from the interpreter only the knowledge of the skeletal outlines of the sources expressed by simple geometric elements such as points and lines. Through these approaches the interpreter specifies a set of skeletal outlines (points and lines) of the presumed sources and the method finds a solution that concentrates the anomalous mass about these skeletons. Therefore, the interpreter is not required to specify the complete source geometry. Calcagno *et al.* (2008) combined the measurements of the structural data on outcrops or in boreholes (e.g. dip measurements, stratifications or foliations related to the contacts) and a set of rules derived from the rock relationships between formations (e.g. the chronology of geological events or different rock relations between formations) with potential field data (gravity and magnetic data). In Calcagno *et al.*'s (2008) approach the judicious combination of geological maps, borehole data, structural data, physical properties of the rocks, gravity and/or magnetic data allows building 3-D geological models.

The reconstruction of 3-D (or 2-D) geological sources through the gravity-inversion methods has been proposed by many authors. Most inversion methods estimate a 3-D density-contrast distribution by assuming a piecewise constant function defined on a user-specified grid of cells. However, the problem of estimating a 3-D (or 2-D) density-contrast distribution from gravity data only is an ill-posed problem because its solution is neither unique nor stable. To transform this ill-posed problem into a well-posed one, these gravity-inversion methods usually use the Tikhonov regularization method (Tikhonov & Arsenin 1977). It consists in formulating a constrained inverse problem by minimizing an unconstrained function composed by (1) the data-misfit function, consisting of a norm of the difference between the observed and predicted data, and (2) the regularizing function defined in the parameter (model) space whose minimization imposes physical or geological attributes on a solution. Two regularizing functions commonly used in geophysics are the zeroth- and first-order Tikhonov regularizations. Both regularizing functions impose a smooth character on the estimated density-contrast distribution and they concentrate the excess (or deficiency) of mass at the borders of the interpretation region, irrespective of the true source depth. Some examples of this tendency are given in Portniaguine & Zhdanov (1999), their figs 1(c), 2(c) and 3(c), Barbosa *et al.* (2002), their fig. 5 and Silva *et al.* (2001a), their figs 7 and 8. Over the last years, efforts have been directed to counteract the tendency of producing a blurred density-contrast distribution concentrated at the borders of the interpretation region. In this context, some non-smoothing regularization functions arose in estimating the density-contrast distribution in the subsurface. Most

of these non-smoothing regularizers retrieve sharper images of geological sources as compared with the smoothing regularizers, but they require larger amount of prior information. Some examples are given by the following authors: Last & Kubik's (1983) method produced compact and homogeneous solutions; Barbosa & Silva (1994) generalized the moment-of-inertia functional proposed by Guillen & Menichetti (1984) and Barbosa *et al.* (1999a) applied it to reconstruct a heterogeneous sedimentary pack; Bertete-Aguirre *et al.* (2002) used TV regularization, whose stabilizing functional is the ℓ_1 -norm of the first-order derivative of the parameters along the horizontal and vertical directions; Portniaguine & Zhdanov (1999) minimized a measure of the total volume within the estimated source in which the physical property gradient is non-null in 3-D gravity inversion; Silva & Barbosa (2006) and Barbosa & Silva (2006) extended Barbosa & Silva's (1994) method for multiple sources with multiple axes and points; Silva Dias *et al.* (2009) proposed an adaptive learning scheme extending Silva & Barbosa's (2006) method to 3-D gravity inversion.

Although the inversion methods that parametrize the Earth's subsurface into a grid of cells (2-D or 3-D) to estimate a density-contrast distribution allow an enormous flexibility because they can estimate arbitrary variations, the usual Tikhonov regularizations of orders zero and one lead to blurred source images whose maximum and minimum estimated values occur at the boundary of the discretized region. To retrieve a sharper image of geological sources, this inversion approach requires a substantial amount of prior information about the source. A second gravity-inversion approach has been adopted by a few authors to obtain estimates of 3-D (or 2-D) geological source through an interpretation model that eliminates most of the above-mentioned difficulties. In this case the interpretation model consists either of a horizontally infinite prism with polygonal cross-section or of a polyhedral body that delineates the contour of, respectively, 2-D or 3-D isolated sources. Hence, the physical property (density contrast) of the body is assumed to be known and the parameters to be estimated are the geometric elements that define the boundary of a polygonal cross-section or a polyhedral body. Moraes & Hansen (2001), for example, approximated the 3-D geological body by a homogeneous polyhedral body and estimated its vertices using the gravity data and the first-order Tikhonov regularization. Silva & Barbosa (2004) inverted the gravity data for the geometry of an isolated causative body by representing it as a 2-D horizontal prism with a polygonal cross-section defined by vertices which are described in polar coordinates referred to an origin inside the source. The parameters to be estimated in this case are the radii associated with the polygon vertices for a fixed number of equally spaced central angles from 0° to 360° . They used a wide variety of constraints to stabilize the solutions and to introduce information about the source shape. Some examples of possible *a priori* information are the isometry, the convexity and the concentration of the mass along preferred directions. Wildman & Gazonas (2009) developed gravity- and magnetic-inversion methods for retrieving the geometries of 2-D or 3-D multiple sources by assuming the knowledge of their physical properties and representing these geometries by a tree-data structure. These authors approximated the geological sources by an interpretation model consisting either of 2-D prisms with polygonal sections or of polyhedral bodies and estimated the sources geometry in two steps. In the first step, the initial geometry consists of a simple rectangle that is iteratively modified by scaling and translation transformations to determine the approximate size and location of the source. Next, an optimizing stage gives a more accurate image of the source by dividing the leaf nodes of the tree into the union of two separate convex polygons along one

or more angles. Luo (2010) proposed a gravity-inversion method to estimate the geometry of isolated 2-D source adopting Bayesian model inference approach which is implemented via the reversible jump Markov chain Monte Carlo algorithm. This method estimates, in the x - z space beneath the Earth's surface, the number of vertices (and their x - and z -coordinates) that describe a 2-D polygonal cross-section and approximately delineate the edges of an isolated 2-D geological source.

In this paper, we present a 3-D gravity-inversion method to estimate the geometry of an isolated source by assuming the knowledge about the density contrast and about the depth to the top. Our method is a generalization of the method developed by Silva & Barbosa (2004) to interpret gravity data produced by a 2-D geological setting. Here, we approximate the 3-D source by an ensemble of 3-D vertical juxtaposed prisms in the vertical direction whose thicknesses and density contrasts are known and their horizontal cross-sections are described by an arbitrary polygon. The horizontal coordinates of the polygon vertices approximately describe the edges of horizontal depth slices of the 3-D geological source and are the unknown parameters of our method. A set of horizontal polygons consisting of vertically stacked prisms sets up the geometry of the 3-D source. The polygon vertices of each prism are described by polar coordinates with an origin within the top of prism. Our method estimates the radii associated with each polygon vertex for a fixed number of equally spaced central angles from 0° to 360° , and the horizontal Cartesian coordinates of an arbitrary origin. To obtain stable estimates we impose constraints on the source shape. The judicious use of first-order Tikhonov regularization on all or just a few parameters allows estimating both vertical and inclined geological bodies whose shapes can be isometric or anisometric. Although the proposed method estimates a stable solution that fits the observed anomaly within the measurement errors, it will depend on the maximum depth of the set of juxtaposed 3-D prisms that set up the interpretation model. To reduce the class of possible solutions compatible with the gravity anomaly, we propose a new criterion based on the curve of the data-misfit measure versus the estimated total-anomalous mass obtained by assigning different tentative values for the maximum depth of the interpretation model. The minimum data-misfit measure in this curve gives the true (or minimum) depth to the bottom of the geological body. Tests conducted with synthetic data show that the method can be of utility in estimating the geometry of both isometric and elongated 3-D isolated sources. The method has also been applied to a real gravity-data set over greenstone rocks in Matsitama, northeastern Botswana. The estimated source fits acceptably the gravity anomaly and retrieves a dipping intrusion having variable dips and strikes and maximum bottom depth of 8 ± 0.5 km. By comparing the interpretations of simulated sources and Matsitama intrusion, we show that the anomaly fit obtained in the Matsitama application is worse than those obtained in the synthetic tests. This poorer fitting obtained in Matsitama application may be related to possible violations of premises assumed by our method. Violations of premises may be associated either with the presence of multiples sources yielding interfering gravity anomalies or with variable density contrast.

2 METHODOLOGY

2.1 Forward problem

Let \mathbf{g}^o be an N -dimensional vector of gravity observations (Fig. 1a) produced by a 3-D outcropping source (or a buried source, but with a

known depth to the top) having arbitrary but unknown closed surface S (Fig. 1b). We assume that the 3-D source is confined to the interior of a finite region \mathcal{R} , defined on the x - y - z space beneath the Earth's surface (Fig. 1b). The z -axis is positive downwards and the x - and y -axes are northward- and eastward-oriented, respectively. We also assume that the density contrast between the geological source and the host rocks is either constant or variable and known. To obtain the 3-D source shape we approximate the volume of the source (dark grey volume in Fig. 1b) by a set of L vertical, juxtaposed 3-D prisms in the vertical direction (light grey prisms, identified by P^k , $k = 1, \dots, L$ in Fig. 1b). The density contrast of each prism, ρ^k , $k = 1, \dots, L$, is assumed constant and known. All prisms have the same constant and known thickness dz and a horizontal cross-section described by an arbitrary and unknown polygon, whose sides approximately describe the edges of a horizontal cross-section of the 3-D geological source. The horizontal coordinates of the polygon vertices of the ensemble of L vertically stacked prisms recover the 3-D geological source and are the first set of parameters to be estimated from the gravity data. The depths to the top and to the bottom of the k th vertical prism are, respectively,

$$z_1^k = z_0 + (k - 1) dz, \quad k = 1, \dots, L, \quad (1a)$$

and

$$z_2^k = z_1^k + dz, \quad k = 1, \dots, L, \quad (1b)$$

where z_0 is a pre-specified depth to the top of the true geological source based on the interpreter's knowledge about the geology of the interpretation area. Fig. 1(c) shows the polygonal cross-section of the k th vertical prism P^k described by M^k vertices (white dots) with the Cartesian coordinates (x_j^k, y_j^k, z_1^k) , $j = 1, \dots, M^k$, $k = 1, \dots, L$. Similarly Silva & Barbosa (2004), instead of describing each vertical prism by the Cartesian coordinates of its vertices, we describe them by polar coordinates referred to an arbitrary origin whose z -coordinate coincides with the depth to the top of the corresponding prism. Then, the horizontal Cartesian coordinates of the M^k vertices, (x_j^k, y_j^k) (white dots in Fig. 1d), of the k th vertical prism P^k , $j = 1, \dots, M^k$, $k = 1, \dots, L$, are described by the polar coordinates (r_j^k, θ_j^k) , $j = 1, \dots, M^k$, $k = 1, \dots, L$ referred to an arbitrary origin O^k (grey dot in Fig. 1d) with horizontal coordinates (x_o^k, y_o^k) , $k = 1, \dots, L$, $\in P^k$. By convention, the angle θ_j^k is measured from the positive y -axis in the counterclockwise sense. Based on the interpreter's knowledge about the complexity of true source (dark grey volume in Fig. 1b), the number of vertices of each prism is established. After setting the value of M^k for the k th vertical prism, we define the set of fixed and equally spaced angles from 0° to 360° by

$$\theta_j^k = (j - 1)\Delta\theta^k, \quad j = 1, \dots, M^k, \quad (2)$$

where

$$\Delta\theta^k = \frac{2\pi}{M^k}, \quad k = 1, \dots, L.$$

Here, to retrieve the 3-D geometry of a geological source we estimate two sets of parameters representing different physical entities. The first set of parameters comprises the radii of all prisms $(r_j^k, j = 1, \dots, M^k, k = 1, \dots, L)$ and the second one includes the horizontal Cartesian coordinates (x_o^k, y_o^k) of the arbitrary origins O^k , $k = 1, \dots, L$.

The vertical component of the theoretical gravity attraction, g_i , at the i th observation point ($x = x_i$, $y = y_i$, and $z = z_i$) caused by a set of L 3-D prisms (light grey prisms in Fig. 1b) is given by the

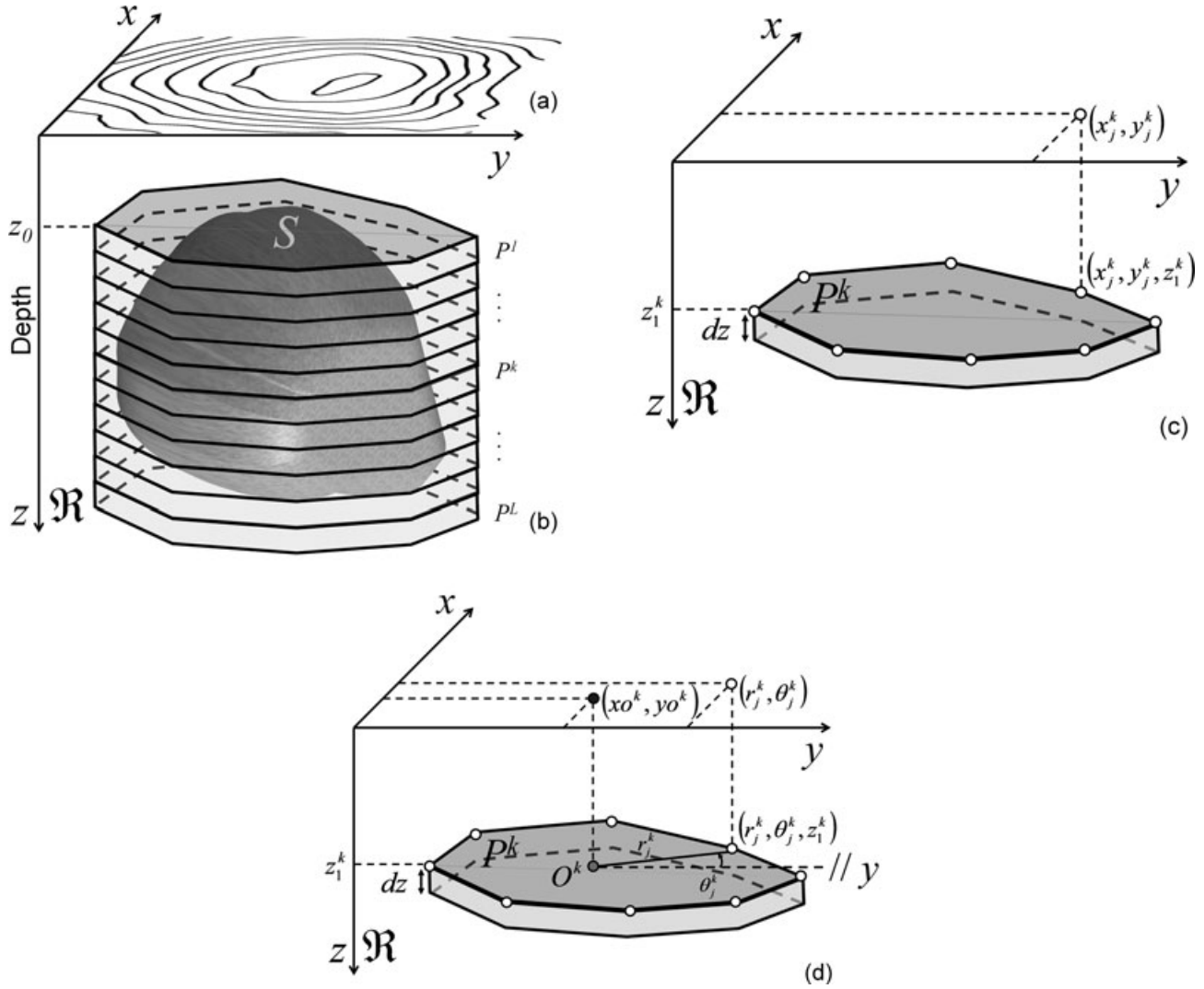


Figure 1. Schematic representation of (a) gravity anomaly (contour lines) produced by (b) a 3-D anomalous source (dark grey volume limited by the closed surface S). The interpretation model in (b) consists of a set of L vertical, juxtaposed 3-D prisms P^k , $k = 1, \dots, L$, (light grey prisms) in the vertical direction of a right-handed coordinate system. (c) Polygonal cross-section of the k th vertical prism P^k described by M^k vertices (white dots) with the Cartesian coordinates (x_j^k, y_j^k, z_1^k) , $j = 1, \dots, M^k$, $k = 1, \dots, L$. (d) Representation of the M^k vertices of the k th vertical prism P^k , (x_j^k, y_j^k) , $j = 1, \dots, M^k$, $k = 1, \dots, L$, by polar coordinates (r_j^k, θ_j^k) , $j = 1, \dots, M^k$, $k = 1, \dots, L$, (white dots), referred to an arbitrary origin O^k (grey dot) with horizontal Cartesian coordinates (x_o^k, y_o^k) , $k = 1, \dots, L$, (black dot).

non-linear relationship

$$g_i \equiv g_i(x_i, y_i, z_i) = \sum_{k=1}^L f_i^k(\mathbf{r}^k, x_o^k, y_o^k, \boldsymbol{\theta}^k, \rho^k), \quad i = 1, \dots, N, \quad (3)$$

where N is the number of gravity measurements, $\mathbf{r}^k \equiv (r_1^k, \dots, r_{M^k}^k)^T$ is the M^k -dimensional vector containing the radial coordinates of the M^k vertices of the k th vertical prism and $\boldsymbol{\theta}^k$ is the M^k -dimensional vector whose j th element is given in eq. (2). The non-linear function $f_i^k(\mathbf{r}^k, x_o^k, y_o^k, \boldsymbol{\theta}^k, \rho^k)$ has been computed based on Plouff (1976) to calculate the gravity effect at the i th observation point (x_i, y_i, z_i) produced by the k th vertical prism with thickness dz , density contrast ρ^k , and whose polygonal cross-section is described by the variables \mathbf{r}^k , $\boldsymbol{\theta}^k$, x_o^k , and y_o^k .

2.2 Estimating the 3-D geometry of a geological source

We formulate an iterative non-linear inversion to estimate a 3-D geometry of a geological source that not only fits the gravity data

but also satisfies a set of specified constraints. From a set of N gravity observations $\mathbf{g}^o \equiv (g_1^o, \dots, g_N^o)^T$, we estimate the parameter vector \mathbf{m} by minimizing the objective function

$$\Gamma(\mathbf{m}) = \psi(\mathbf{m}) + \mu \sum_{\ell=1}^{LC} \phi^\ell(\mathbf{m}), \quad (4)$$

subject to

$$\mathbf{m}_{\min} < \mathbf{m} < \mathbf{m}_{\max}, \quad (5)$$

where functions $\psi(\mathbf{m})$ and $\phi^\ell(\mathbf{m})$ will be defined later. The M -dimensional parameter vector \mathbf{m} contains the radii of all prisms $(r_j^k, j = 1, \dots, M^k, k = 1, \dots, L)$ and the horizontal Cartesian coordinates (x_o^k, y_o^k) of arbitrary origins O^k , $k = 1, \dots, L$, of all prisms. Hence, the number of unknown parameters to be estimated is $M = \sum M^k + 2L$. We partition the parameter vector as

$$\mathbf{m} = \left(\mathbf{m}^1{}^T \mathbf{m}^2{}^T \dots \mathbf{m}^L{}^T \dots \mathbf{m}^{2L}{}^T \right)^T, \quad (6)$$

where T is the transposition operator and \mathbf{m}^k is the $(M^k + 2) \times 1$ vector whose elements are (1) the radii of the M^k vertices of the k th vertical prism and (2) the horizontal Cartesian coordinates of the k th arbitrary origin, that is,

$$\mathbf{m}^{kT} \equiv (r_1^k, \dots, r_{M^k}^k, x o^k, y o^k) \equiv (\mathbf{r}^k, x o^k, y o^k), \quad k = 1, \dots, L. \quad (7)$$

The minimizer $\hat{\mathbf{m}}$ of the function $\Gamma(\mathbf{m})$ (eq. 4) will be obtained iteratively by the Gauss–Newton method using Marquardt’s (1963) strategy (Silva *et al.* 2001b). From now on, we use the caret (^) symbol to denote estimate. To incorporate the inequality constraints given in inequality (5), we used a homeomorphic transformation (e.g. Barbosa *et al.* 1999b), which has a simple implementation.

The role of the inequality constraints given in inequality (5) is to set physical limits for the estimates of the radii of all vertices of all prisms ($r_1^k, \dots, r_{M^k}^k, k = 1, \dots, L$) and for the estimates of the horizontal Cartesian coordinates of all arbitrary origins ($x o^k, y o^k, k = 1, \dots, L$). For simplicity, we assign the value zero and r_{\max} , respectively, to the lower and upper bounds of all radii, where r_{\max} is set by the interpreter based on either the horizontal extent of the gravity anomaly or the geological knowledge about the studied area. We also assign the values ($x o_{\min}, y o_{\min}$) and ($x o_{\max}, y o_{\max}$), respectively, to the lower and upper bounds of all horizontal Cartesian coordinates of all arbitrary origin.

The function $\psi(\mathbf{m})$ in eq. (4) is the data-misfit function, given by

$$\psi(\mathbf{m}) = \frac{1}{N - M} \sum_{i=1}^N [g_i^o - g_i]^2. \quad (8)$$

Let $\phi^\ell(\mathbf{m})$, $\ell = 1, \dots, LC$, be a set of model objective functions (eq. 4) which allow incorporating different types of prior information into the inverse problem solution. Each model objective function $\phi^\ell(\mathbf{m})$ represents the ℓ th constraint based on a factual geological attribute about the source geometry. Finally, μ is the regularizing parameter that balances the relative importance between the data-misfit measure [given by $\psi(\mathbf{m})$, eq. 8] and the set of constraints given by the model-objective functions, $\phi^\ell(\mathbf{m})$, $\ell = 1, \dots, LC$. In our method, we introduced six types of constraints.

(1) Smoothness constraint on the adjacent radii defining the horizontal section of each vertical prism. This constraint imposes that all radii within each vertical prism must be close to each other. Specifically, it consists of requiring that the estimate of each radius \hat{r}_j^k (the j th radius within the k th vertical prism) be as close as possible to the estimate of radius \hat{r}_{j+1}^k (the neighbouring radius within the k th vertical prism). In other words, within each vertical prism, an abrupt change between a given radius and its neighbour is ruled out. Mathematically, this constraint is expressed by the squared ℓ_2 -norm of the first-order discrete derivative (along the azimuthal direction) of the radii defining the horizontal section of each vertical prism:

$$\phi^1(\mathbf{m}) = \alpha_1 \sum_{k=1}^L \left[(r_{M^k}^k - r_1^k)^2 + \sum_{j=1}^{M^k-1} (r_{j+1}^k - r_j^k)^2 \right]. \quad (9a)$$

This constraint is a regularizing function applied to all radii within each vertical prism of the interpretation model and it is named as the first-order Tikhonov regularization (Tikhonov & Arsenin 1977). This constraint favours solutions composed of vertical prisms defined by approximately circular cross-section. Then, the estimated source shape is biased to be piecewise horizontally isometric.

(2) Smoothness constraint on the adjacent radii of the vertically adjacent prisms. Let us assume for simplicity that all prisms have the same number of vertices, that is, $M^k = M^o$, $k = 1, \dots, L$, this

constraint imposes that the pairs of adjacent radii of two vertically adjacent prisms must be close to each other. It is incorporated by minimizing

$$\phi^2(\mathbf{m}) = \alpha_2 \sum_{k=1}^{L-1} \sum_{j=1}^{M^o} (r_j^k - r_j^{k+1})^2, \quad (9b)$$

where r_j^k and r_j^{k+1} define a pair of adjacent radii of the k th and $k+1$ st vertical prisms. Mathematically, eq. (9b) expresses the squared ℓ_2 -norm of the discrete first-order derivative of the radii along the vertical direction. It represents the first-order Tikhonov regularization on the radii of vertically adjacent prisms of the interpretation model. Then, this constraint favours solutions with a vertically cylindrical shape.

(3) The source’s outcrop constraint. In the case of outcropping sources, let’s assume that the intersection of the geological source with a horizontal erosion surface is known. This constraint incorporates prior knowledge about the outcropping source’s boundaries separating the geological body from the host rock. Mathematically, it imposes that the estimated radii and the arbitrary origin of the shallowest vertical prism ($\hat{r}_1^1, \dots, \hat{r}_{M^1}^1, \hat{x} o^1, \hat{y} o^1$), which describe the boundary of the polygonal cross-section of the first vertical prism P^1 , must be as close as possible to the pre-specified values ($r_1^0, \dots, r_{M^1}^0, x o^0, y o^0$), which describe the known outcropping boundary separating the anomalous source from the host rock). This constraint is incorporated by minimizing

$$\phi^3(\mathbf{m}) = \alpha_3 \left\{ \left[\sum_{j=1}^{M^1} (r_j^1 - r_j^0)^2 \right] + (x o^1 - x o^0)^2 + (y o^1 - y o^0)^2 \right\}. \quad (9c)$$

(4) The source’s horizontal location constraint. Let’s assume that the interpreter does not have information about the outcropping boundary of the body in greater detail, but he knows the approximate horizontal Cartesian coordinates of body ($x o^o, y o^o$). In this case, the constraint given in eq. (9c) must be simplified to minimize

$$\phi^4(\mathbf{m}) = \alpha_4 \left[(x o^1 - x o^o)^2 + (y o^1 - y o^o)^2 \right]. \quad (9d)$$

(5) Smoothness constraint on the horizontal position of the arbitrary origins of the vertically adjacent prisms: This constraint imposes that the estimate of the horizontal position of the k th arbitrary origin O^k , at the k th vertical prism P^k , must be as close as possible to the estimate of spatially adjacent arbitrary origin O^{k+1} , at the $k+1$ st vertical prism P^{k+1} . Mathematically, this constraint imposes that the estimated horizontal Cartesian coordinates ($\hat{x} o^k, \hat{y} o^k$) of the k th arbitrary origin O^k must be as close as possible to the estimated horizontal Cartesian coordinates ($\hat{x} o^{k+1}, \hat{y} o^{k+1}$) of the vertically adjacent arbitrary origin O^{k+1} . This constraint is imposed by minimizing the function

$$\phi^5(\mathbf{m}) = \alpha_5 \sum_{k=1}^{L-1} (x o^{k+1} - x o^k)^2 + (y o^{k+1} - y o^k)^2. \quad (9e)$$

This regularizing function is the first-order Tikhonov regularization on the horizontal position of the arbitrary origins of the vertically adjacent prisms and it imposes smooth horizontal displacement between all vertically adjacent prisms.

(6) Minimum Euclidean norm constraint on the adjacent radii within each vertical prism. This constraint imposes that all radii within each vertical prism must be as close as possible to null values. This constraint, known as minimum Euclidean norm, is expressed

by the squared ℓ_2 - norm of the radii describing each vertical prism

$$\phi^6(\mathbf{m}) = \alpha_6 \sum_{k=1}^L \sum_{j=1}^{M^k} (r_j^k)^2. \quad (9f)$$

In our method, this constraint has been used to guarantee a stable solution.

Here, we adopted the following strategy for selecting the control parameters (μ and $\alpha_1 - \alpha_6$). We set the regularizing parameter μ (eq. 4) equal to unity in all inversions. In the functions given in eqs (9a)–(9f) the non-negative coefficients $\alpha_1 - \alpha_6$ enable the appropriate balance between the six constraining functions $[\phi^1(\mathbf{m}) - \phi^6(\mathbf{m})]$ in a particular problem. These constraining functions are used to reduce solution non-uniqueness and instability. To date, the coefficients $\alpha_1 - \alpha_6$ cannot be estimated automatically. Roughly, each coefficient defines how much of the information defined by the corresponding constraining function should be incorporated into the solution. This information must be essentially provided by geological knowledge. Thus, the choice of these coefficients is based on the trial-and-error procedure and on the interpreter's knowledge about the geology of the study area, except for α_6 . Because function $\phi^6(m)$ is used as a mathematical stabilizing constraint only, we set a very small value (on the order of 10^{-5}) to α_6 .

2.3 Estimating stable solutions

In simple, non-mathematical terms, stable solution is a solution that is only slightly perturbed when the observations are contaminated by small-amplitude random perturbations. To obtain a stable solution we adopted the following practical procedure. First, we generate Q sets of noise-corrupted gravity data by adding Q different Gaussian pseudo-random noise sequences with zero mean. Next, we set up the variables of the interpretation model (see Section 2.1), the constraining functions (eqs 9a–9f) and the associated inversion control parameters (variables $\alpha_1 - \alpha_6$ and μ , described in Section 2.2). Then, we invert the Q sets of noise-corrupted gravity data using the specified variables $\alpha_1 - \alpha_6$ to obtain a set of Q estimates $\hat{\mathbf{m}}_1, \dots, \hat{\mathbf{m}}_Q$, that minimize the function $\Gamma(\mathbf{m})$ (eq. 4) subject to the inequality constraints given in inequality (5). Finally, we compute the sample mean and the sample standard deviation, of the set of Q values, obtained though inversion, for the set of the j th elements of $\hat{\mathbf{m}}_k$, $k = 1, \dots, Q$, using, respectively, the equations

$$\tilde{m}_j = \frac{1}{Q} \sum \hat{m}_{kj}, \quad j = 1, \dots, M, \quad (10)$$

and

$$\tilde{\sigma}_j = \left[\frac{1}{Q-1} \sum (\hat{m}_{kj} - \tilde{m}_j)^2 \right]^{1/2}, \quad j = 1, \dots, M, \quad (11)$$

where \hat{m}_{kj} is the j th element of the k th estimated parameter vector $\hat{\mathbf{m}}_k$.

The sample mean parameter vector $\tilde{\mathbf{m}}$, whose j th element is given by eq. (10), may be accepted as an estimated solution of the inverse problem, depending on whether $\tilde{\mathbf{m}}$ is a stable estimate. The estimated sample mean parameter vector $\tilde{\mathbf{m}}$ is assumed to be stable when all sample standard deviations ($\tilde{\sigma}_j$, $j = 1, \dots, M$) are smaller than 4 per cent of its corresponding sample mean. Otherwise, the estimated parameter vector $\tilde{\mathbf{m}}$ is rejected, the inversion control parameters are modified and a new inversion is started. This process is repeated until all sample standard deviations attain small values.

In this paper, we use this procedure to evaluate the stability of the solution either in synthetic or real gravity anomalies. In all

applications presented in this paper, we set $Q = 30$ and use the stable sample mean parameter vector $\tilde{\mathbf{m}}$ (eq. 10) as the stable estimated solution (or stable estimated parameter vector). Finally, we compute the fitted gravity anomaly produced by $\tilde{\mathbf{m}}$.

3 CRITERION FOR ESTIMATING THE TRUE (OR MINIMUM) DEPTH TO THE BOTTOM OF THE SOURCE

In Section 2.1, we established the discretization of a finite region \mathcal{R} into a set of L prisms (Fig. 1b), with a constant and known thickness dz . The shallowest prism has the depth to the top equal to z_0 that presumably coincides with the top of the true geological source. These variables (L , dz and z_0) define the maximum depth to the bottom of the estimated body by

$$z_{\max} = z_0 + L \cdot dz. \quad (12)$$

After setting up the interpretation model, our method obtains a stable estimate of the 3-D geometry of the source by applying the practical procedure described in the Section 2.3. Besides being stable, the solution $\tilde{\mathbf{m}}$ must yield an acceptable anomaly fit.

For a fixed maximum depth to the bottom of the interpretation model z_{\max} , we obtain a stable estimate $\tilde{\mathbf{m}}$ that fits the data. However, this estimate depends on z_{\max} ; so, by assigning different values to z_{\max} , the method produces other stable solutions $\tilde{\mathbf{m}}$ that fit the data as well. To overcome this vexatious dependence of the solution on the correct choice of the maximum bottom depth for the true body, we developed a new criterion for reducing the class of possible solutions compatible with the gravity anomaly by estimating an 'optimum' maximum depth to the bottom of the interpretation model. This optimum maximum depth can be an estimate of the true (or minimum) depth to the bottom of the source, depending on whether the true source produces a gravity anomaly that is able (or unable) to resolve the depth to the source bottom. This new criterion is based on the fact that an increase of the thickness (dz) of the prisms defining the interpretation model leads to an increase of its depth to the bottom and allows an increase of the estimated source volume, and, therefore, of the total-anomalous mass (m_t). By calculating m_t and adopting a convenient data-misfit measure (s), we construct a curve m_t versus s . This curve is used to estimate an optimum maximum depth to the bottom of the interpretation model and, consequently, the depth-to-bottom estimate of the source.

3.1 Relationship between the data-misfit measure and the estimated total-anomalous mass

The total anomalous mass (Hammer 1945; LaFehr 1965; Blakely 1995) can be calculated from an application of Gauss' theorem. Assume that the vertical component of the gravity attraction $g_z(x, y, z)$ is known in a continuous way over an infinite horizontal surface S_p , located above all anomalous masses causing $g_z(x, y, z)$. Hence, the vertical component of gravity integrated over S_p is proportional to the total-anomalous mass, that is,

$$m_t = \frac{1}{2\pi\gamma} \iint_{S_p} g_z(x, y, z) ds, \quad (13)$$

where γ is Newton's gravitational constant.

Because the measured or computed vertical component of gravity $g_z(x, y, z)$ is not obtained continuously over an infinite plane, but as a discrete set of N gravity observations, distributed over a finite plane, the integral in eq. (13) must be numerically approximated

by finite sums. Let $\mathbf{g} \equiv (g_1, \dots, g_N)^T$ be a set of N fitted gravity observations produced by the stable estimated solution $\hat{\mathbf{m}}$ (see the Section 2.3). Let us consider a sufficiently dense set of gravity data such as the integral in eq. (13) can be numerically approximated by

$$m_t \approx \frac{1}{2\pi\gamma} \sum g_i ds_i, \quad (14)$$

where ds_i is the i th horizontal element of area and m_t will henceforth be referred to as estimated total-anomalous mass.

On the other hand, we define a data-misfit measure as

$$s = \frac{1}{N} \sum |(g_i^o ds_i) - (g_i ds_i)| = \frac{1}{N} \sum |a_i - b_i|, \quad (15)$$

where $a_i = g_i^o ds_i$ and $b_i = g_i ds_i$. So, given a vector of parameter estimates $\hat{\mathbf{m}}$ which yields a vector of fitted gravity data $\mathbf{g} \in \{g_i, i = 1, \dots, N\}$, the total-anomalous mass can be approximated by the expression

$$m_t \approx \kappa \sum b_i, \quad (16)$$

where $\kappa = 1/2\pi\gamma$.

In deducing the relationship between the data-misfit measure (eq. 15) and the approximation of the estimated total-anomalous mass (eq. 16), we consider two extreme possibilities. In the first one, let's assume that $b_i < a_i$, for all observation point i . In this case, the fitted gravity data underestimate the observed gravity data (Fig. 2a) and the data-misfit measure (eq. 15) can be rewritten as

$$s = \frac{1}{N} \sum |a_i| - \frac{1}{N} \sum |b_i|. \quad (17)$$

By inserting the form of the approximate estimate of total-anomalous mass (eq. 16) into the data-misfit measure defined by eq. (15), we have the first relationship between the data-misfit measure and the estimated total-anomalous mass, that is,

$$m_t \approx \kappa \sum |a_i| - (N\kappa)s. \quad (18)$$

The above equation shows a linear relationship between the estimated total-anomalous mass m_t and the data-misfit measure s with a negative angular coefficient. Hence, m_t increases as s decreases.

In the second possibility, let us assume that $b_i > a_i$, for all observation point i . In this case, the fitted gravity data overestimate the observed gravity data (Fig. 2b) and the data-misfit measure (eq. 15) can be rewritten as

$$s = \frac{1}{N} \sum |b_i| - \frac{1}{N} \sum |a_i|. \quad (19)$$

By inserting the form of the approximate estimate of total-anomalous mass (eq. 16) into the data-misfit measure defined by eq. (19), we have the second relationship between the data-misfit measure and the estimated total-anomalous mass, that is,

$$m_t \approx \kappa \sum |a_i| + (N\kappa)s. \quad (20)$$

The above equation shows a second linear relationship between the estimated total-anomalous mass m_t and the data-misfit measure s with a positive angular coefficient. Hence, m_t increases with increasing s .

Note that the deduced relationships between the estimated total-anomalous mass (m_t) and the data-misfit measure (s) can be approximated as straight lines (eqs 18 and 20). These two straight lines intercept each other if and only if s is equal to zero. In this case, the observed gravity data are perfectly fitted (Fig. 2c) and the estimated total-anomalous mass (m_t) is approximately equal to the computed total-anomalous mass M_T from the observed gravity data, that is,

$$m_t \approx \kappa \sum |a_i| \approx \frac{1}{2\pi\gamma} \sum g_i^o ds_i \approx M_T. \quad (21)$$

Fig. 2d shows a schematic representation on the plane $m_t \times s$ of the theoretical straight lines I and II given by eqs 18 and 20, respectively. The intersection point of these straight lines is indicated by a black dot, in Fig. 2(d). The graph shown in Fig. 2(d) will be referred to as theoretical $m_t \times s$ curve.

3.2 Departure from the predicted relationship between the data-misfit measure s and the estimated total-anomalous mass m_t in the neighbourhood of $s = 0$

We have deduced two linear relationships (eqs 18 and 20) between the data-misfit measure (s) and the estimated total-anomalous mass (m_t) given a stable parameter estimate $\hat{\mathbf{m}}$. We have also deduced that the intersection point of these straight lines occurs when s is exactly equal to zero. In this section, we analyse the departure of the intersection point of the straight lines from $s = 0$, and the departure of the relationship between m_t and s from a straight line in the neighbourhood of $s = 0$.

Let q be a non-negative number representing the smallest data-misfit value still fitting the data. If q is equal to zero the intersection point of the straight lines (eqs 18 and 20) occurs at $s = 0$; otherwise it departs from $s = 0$. Three factors contribute to this departure. The first one is the presence of noise in data. The second one is the decrease of the gravity data power to resolve very deep source's bottoms. The third factor is the inadequacy of the interpretation model to retrieve the geological body. Then, if q is different from zero, eq. (15) becomes

$$s = \frac{1}{N} \sum |(g_i^o ds_i) - (g_i ds_i)| = \frac{1}{N} \sum |a_i - b_i| + q. \quad (22)$$

Consequently, the two linear relationships between s and m_t given by eqs (18) and (20) will be modified to

$$m_t \approx \kappa \sum |a_i| - (N\kappa)s + (N\kappa)q, \quad (23)$$

and

$$m_t \approx \kappa \sum |a_i| + (N\kappa)s - (N\kappa)q, \quad (24)$$

respectively. In this case, the intersection point of these straight lines (eqs 23 and 24) occurs at $s = q$. It will, therefore, be displaced towards the positive s -axis when $s > 0$.

In the neighbourhood of the point $s = q$, the relationship between m_t and s will depart from the predicted straight lines (eqs 18 and 20) because of the presence of noise in data and of the inadequacy of the interpretation model to retrieve the geological body leading to violation of conditions $a_i < b_i$ and $a_i > b_i$, for all observation points i (Fig. 2e). These conditions are necessary to guarantee the straight line behaviour described by eqs 15 and 18.

3.3 Practical procedure to determine the true (or minimum) depth to the bottom of the source through the $m_t \times s$ curve

To determine the true (or minimum) depth to the source's bottom, we first need to understand the relationship between the $m_t \times s$ curve with the maximum depth of the interpretation model (z_{\max} , eq. 12) and the true (or minimum) depth to the source's bottom. This approach is valid only if the gravity anomaly is caused by an isolated body with a homogeneous density contrast with the host rocks and having a known depth to the top.

First, consider the following theoretical statements. Assume that a homogeneous source with maximum depth to the bottom at z^b

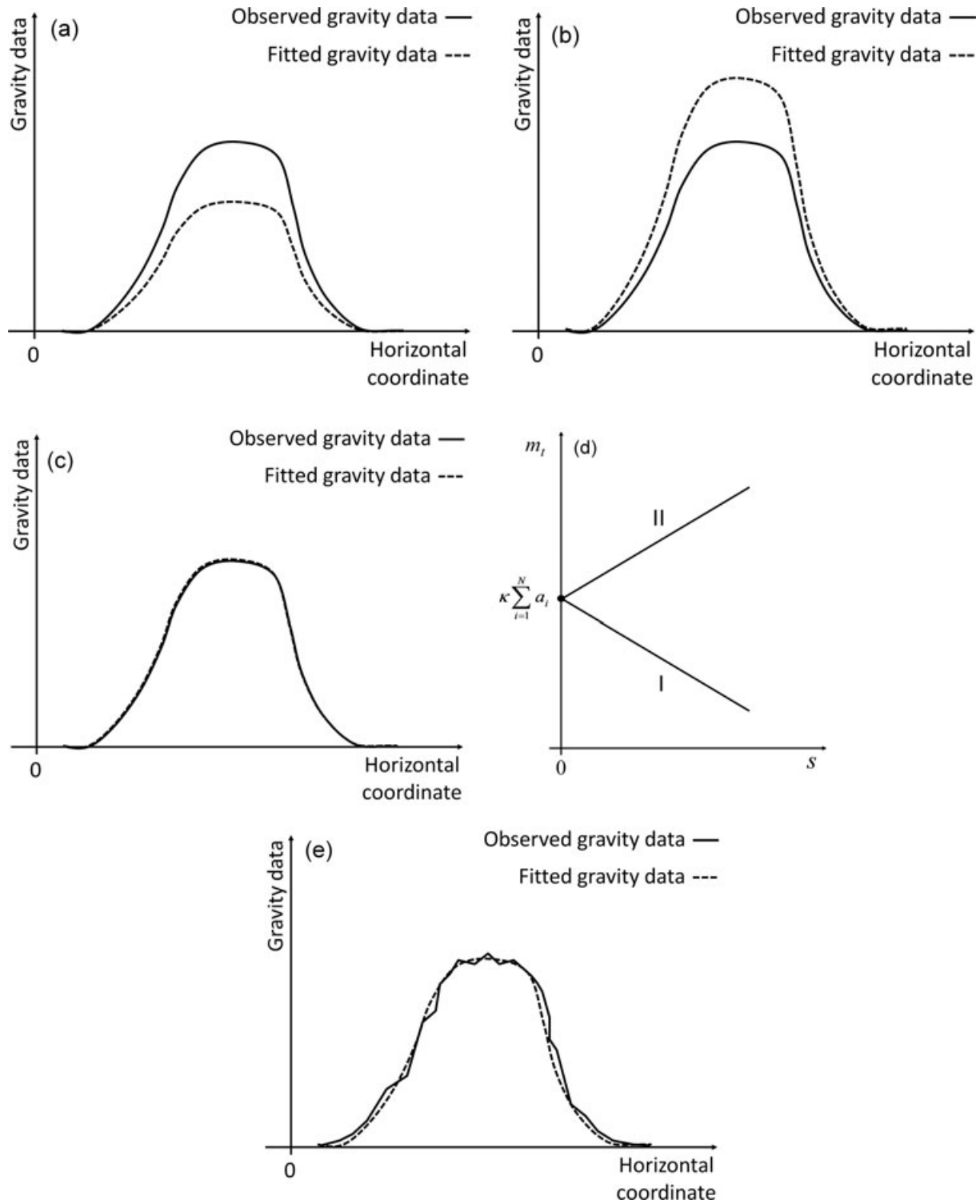


Figure 2. Schematic representation of the observed and fitted gravity data. The fitted gravity data (a) underestimate, (b) overestimate and (c) correctly estimate the observed gravity data. (d) Theoretical $m_t \times s$ curve whose straight lines I and II are given by eqs (18) and (20), respectively. The intersection point of these straight lines occurs at $s = 0$ (black dot).

produces a gravity anomaly $w^o(x, y)$. If this source is modified by removing mass from its bottom up to z_1^b ($z_1^b < z^b$), then this new source will produce a gravity anomaly $w(x, y) < w^o(x, y), \forall x, y$ because no matter how small, the removed mass will add a negative gravity effect measured on all observation locations. Similarly, if the original source is modified by accruing mass to its bottom up to

z_2^b ($z_2^b > z^b$), then this new source will produce a gravity anomaly $w(x, y) > w^o(x, y), \forall x, y$.

Now we extend the above statements to the construction of the $m_t \times s$ curves. This is possible because the $m_t \times s$ curves are produced through the proposed method which assumes homogenous sources and allows either the removal or the accretion of masses

at the bottom of different tentative solutions simply by defining the maximum depth, z_{\max} , of the interpretation model. If z_{\max} is smaller than the true depth to the bottom of the source, the fitted gravity data (produced by a solution using the proposed method) underestimate the observed gravity data (as shown in Fig. 2a) and lead to the theoretical straight line I approximation (Fig. 2d) on the $m_t \times s$ plane. Conversely, if z_{\max} is greater than the true depth to the bottom of the source, the fitted gravity data (produced by a solution using the proposed method) overestimate the observed gravity data (Fig. 2b) and lead to the theoretical straight line II approximation (Fig. 2d) on the $m_t \times s$ plane. Finally, if z_{\max} coincides with the true depth to the bottom of the source, the fitted gravity data (produced by a solution using the proposed method) are approximately equal to the observed gravity data (Fig. 2c) and a minimum value of the data-misfit measure s (such as the one shown schematically by a black dot in Fig. 2d), is expected. In this way, by varying the maximum depth of the interpretation model (z_{\max} , eq. 12) we construct an observed $m_t \times s$ curve similar to the theoretical $m_t \times s$ curve (Fig. 2d). The tentative value for z_{\max} producing the smallest data-misfit measure s on the observed $m_t \times s$ curve is an optimum estimate of the true (or minimum) depth to the bottom of the source.

Here, we do not compute the estimated total-anomalous mass m_t by eqs (14) or (16). Rather, it is computed from the stable parameter estimates $\hat{\mathbf{m}}$ (see the Section 2.3). So, by assuming the correct knowledge of the density contrast between the geological source and the host rock, we first calculate the area of the estimated horizontal section of the k th vertical prism by computing one half of the magnitude of the cross product between two estimated adjacent radius,

$$a^k = \frac{1}{2} [(\hat{x}_{M^k}^k - \hat{x}_O^k)(\hat{y}_1^k - \hat{y}_O^k) - (\hat{x}_1^k - \hat{x}_O^k)(\hat{y}_{M^k}^k - \hat{y}_O^k)]^{1/2} + \sum_{j=1}^{M^k-1} \frac{1}{2} [(\hat{x}_j^k - \hat{x}_O^k)(\hat{y}_{j+1}^k - \hat{y}_O^k) - (\hat{x}_{j+1}^k - \hat{x}_O^k)(\hat{y}_j^k - \hat{y}_O^k)]^{1/2}, \quad (25)$$

where \hat{x}_j^k and \hat{y}_j^k , $i = 1 \dots M^k$, are the horizontal Cartesian coordinates of the M^k vertices, (white dots in Fig. 1d) obtained from the estimated radii of the M^k vertices of the k th vertical prism and \hat{x}_O^k and \hat{y}_O^k are the estimated horizontal Cartesian coordinates of the k th arbitrary origin O^k (grey dot in Fig. 1d). Then, the exact expression of the estimated total-anomalous mass is written as

$$m_t = dz \sum_{k=1}^L \rho^k a^k. \quad (26)$$

The practical procedure to construct the observed $m_t \times s$ curve is as follows. First, we assign a small value to z_{\max} that defines the initial interpretation model. Then, we compute the stable estimated solution $\hat{\mathbf{m}}$ (see Section 2.3) whose j th element is given by eq. (10). Next, we compute the fitted gravity data produced by $\hat{\mathbf{m}}$ that allows computing the data-misfit measure s (eq. 15) and the estimated total-anomalous mass m_t (eq. 26). Finally, we plot m_t against s , producing the first point of the observed $m_t \times s$ curve. We repeat this procedure for increasingly larger values of maximum depths z_{\max} of the interpretation model.

3.4 Illustration of the practical procedure to determine the true (or minimum) depth to the bottom of the source through the $m_t \times s$ curve

We illustrate how the true (or minimum) depth to the bottom of the source can be estimated from the observed $m_t \times s$ curve. To do

this, we simulated three outcropping dipping volcanic ducts with a density contrast ρ of 0.5 g cm^{-3} relative to the background and differing from each other by their maximum depth to the bottom. The first one is a shallow-bottomed dipping duct which attains a maximum bottom depth of 3 km (Figs 3a–c red prisms). The second simulation consists of a middle-bottomed dipping duct with bottom depth of 6 km (not shown). The third simulation involves a deep-bottomed dipping duct whose maximum bottom depth is 9 km (Figs 4a–c in red prisms). For each simulation, we computed, on the plane $z = 0 \text{ km}$, the theoretical noise-free (not shown) and the noise-corrupted gravity data. Figs 3(a)–(c) and 4(a)–(c) show, in half-tone maps, the noise-corrupted gravity data produced, respectively, by shallow- and deep-bottomed dipping volcanic ducts.

In all inversions, we set $z_0 = 0 \text{ km}$ because we simulated outcropping dipping volcanic ducts and assumed that the depths to the tops of the interpretation models coincide with the actual tops of the sources. To all interpretation models we set an ensemble of $L = 5$ prisms, all of them with the same density contrast and the same number of polygon vertices that describe the horizontal cross-sections. Specifically, to all prisms we set $\rho^k = \rho = 0.5 \text{ g cm}^{-3}$ and $M^k = 4$, for all k , $k = 1, \dots, L$. We used all the constraining functions described in the Section 2, except for the third constraint (named source's outcrop constraint, see eq. 9c).

For each simulated test, we followed the same practical procedure described in the Section 3.3, but built two sets of observed $m_t \times s$ curves. The first one is obtained by using the noise-free data (Fig. 5a) and second set of $m_t \times s$ curves is obtained by using the noise-corrupted data (Fig. 5b). Each $m_t \times s$ curve is composed by 11 estimated values of m_t and s , each one associated with a fixed maximum depth z_{\max} of the interpretation model, in which the value of z_{\max} varies from 1 km to 11 km by steps of 1 km. This step implies that the uncertainty in the estimated true (or minimum) depth to the bottom of the source is at most $\pm 0.5 \text{ km}$. Fig. 5 shows the observed $m_t \times s$ curves obtained for the three simulated tests where the dots correspond to different values of maximum depths z_{\max} assumed for the interpretation models.

Although the observed $m_t \times s$ curves (Fig. 5) are different from the theoretical behaviour of the $m_t \times s$ curve (Fig. 2d), they show two asymptotic linear relationships between the estimated total-anomalous mass m_t and the data-misfit measure s , one with a negative and the other with a positive angular coefficient, in accordance with the theoretical results given by eqs (18) and (20), respectively.

In the case of the shallow-bottomed dipping duct, the minima of s are very well defined in the observed $m_t \times s$ curves, shown in blue lines, both for noise-free (Fig. 5a) and noise-corrupted (Fig. 5b) data. These minima are well defined because the gravity anomaly produced by this shallow-bottomed source is able to estimate, under the imposed constraints, the true maximum depth of the source producing the minimum of s . According to the theoretical derivation presented in Section 3.1, the tentative value for the maximum depth z_{\max} producing the minimum of the data-misfit measure s (see the blue lines in Fig. 5) is the best estimate of the true depth to the bottom of the simulated shallow-bottomed dipping duct, both for noise-free and noise-corrupted data. The best estimate of the true depth to the bottom of this source is $z_{\max} = 3 \pm 0.5 \text{ km}$ which agrees with the true one. Fig. 3(b) shows that the estimated 3-D geometry of the source (blue prisms) using the maximum depth $z_{\max} = 3 \text{ km}$ recovers very well the geometry of the true shallow-bottomed dipping duct. The corresponding fitted anomaly is displayed in Fig. 3(b) in dashed black lines. Figs 3(a) and (c) show the estimated 3-D geometries of the source (blue prisms) using smaller ($z_{\max} = 2 \text{ km}$) or larger ($z_{\max} = 4 \text{ km}$) maximum depth to the bottom z_{\max} of the

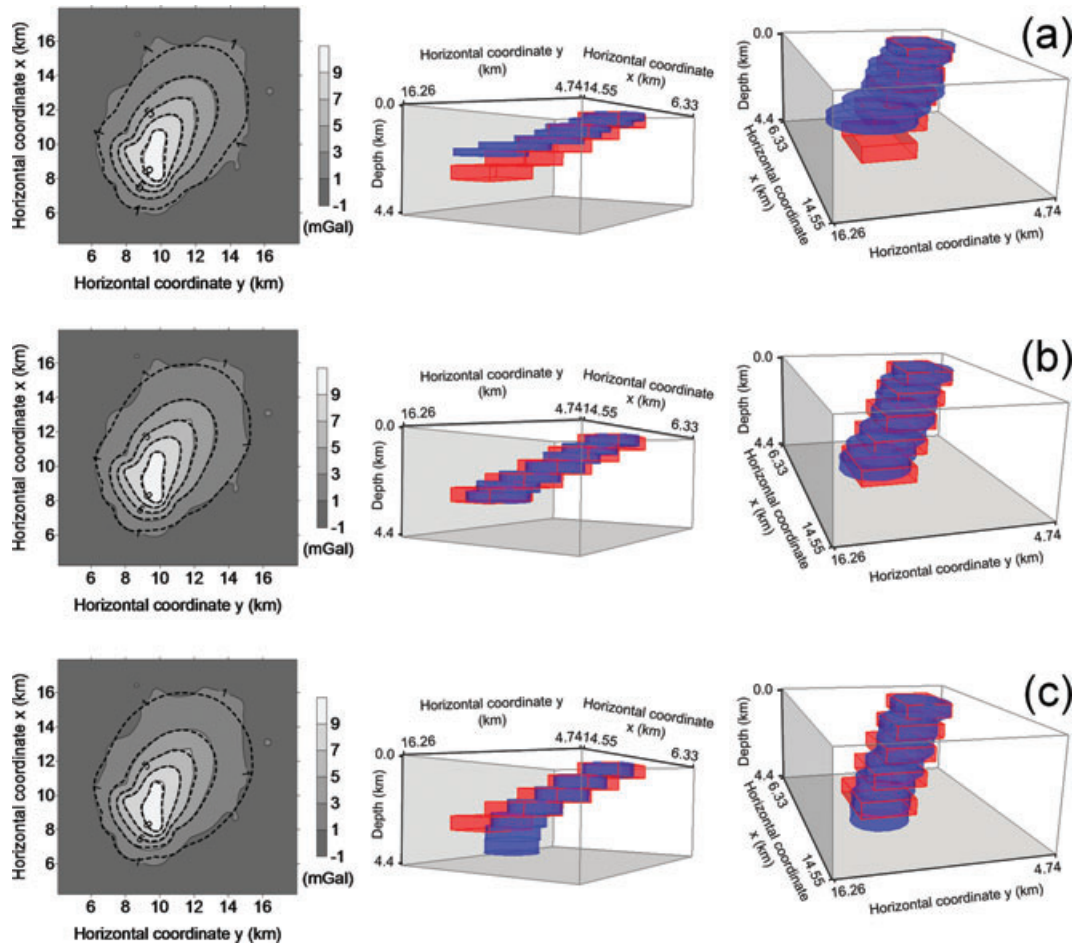


Figure 3. Synthetic data application produced by a simulated outcropping dipping volcanic duct. Perspective views of the true (red prisms) and estimated (blue prisms) shallow-bottomed dipping duct; the latter is obtained by inverting the noise-corrupted gravity data (half-tone contour map) and assuming an interpretation model with maximum bottom depths z_{\max} (a) smaller (2 km); (b) equal (3 km) and (c) larger (4 km) than the true one. The corresponding fitted gravity anomalies produced by the estimated sources (blue prisms in a–c) are shown in dashed black lines in the contour maps (a)–(c).

interpretation models relative to the true one. In this case, neither estimated 3-D geometry of the sources (blue prisms in Figs 3a and c) recover the true geometry of the shallow-bottomed dipping duct (red prisms), even though both solutions fit the gravity observations (dashed black lines in Figs 3a and c). In the case of the deep-bottomed dipping duct, the minimum of s is reasonable, defined by the $m_t \times s$ curve obtained for noise-free data (green line in Fig. 5a). On the other hand, the noise-corrupted gravity data produced by the deep-bottomed dipping duct do not have enough resolution to define the smallest value of s in the $m_t \times s$ curve (green line in Fig. 5b) and, consequently, to produce reliable estimates of the true maximum depth of the source. So, the ambiguous smallest value of s in the $m_t \times s$ curve (green line in Fig. 5b) indicates the impossibility of determining the true maximum depth of the source. In this case, this $m_t \times s$ curve can be used to estimate, at most, a lower bound ($z_{\max} = 6 \pm 0.5$ km) for the maximum depth of the source. The loss of resolution of the gravity data with depth leads to the impossibility of retrieving the 3-D geometry of the deepest part of the true source (red prisms) as shown in Figs 4(a)–(c); however, the shallowest part of the true source geometry is reasonably retrieved. In Figs 4(a)–(c) the maximum depth z_{\max} , assumed for the interpretation models, are, respectively, smaller ($z_{\max} = 8$ km), equal ($z_{\max} = 9$ km) and larger ($z_{\max} = 10$ km) than the true one. Neither estimated geometries (blue prisms in Figs 4a–c) perfectly

recovered the true dipping volcanic duct (red prisms in Figs 4a–c), even though all of them fit the gravity data (dashed black lines in Figs 4a–c) and are stable. These unsatisfactory results, even using an interpretation model whose maximum depth of the interpretation model coincides with the true one (Fig. 4b), are expected because of the inevitable loss of data resolution with depth. The gravity data lack the necessary in depth resolution and this low resolution makes it impractical to estimate the deepest portion of the source without using prior information (e.g. Silva Dias *et al.* 2009).

Some striking features in Fig. 5 deserve attention. First, the theoretical linear behaviour of the $m_t \times s$ curve at its extremities, shown schematically in Fig. 2(d) has been confirmed numerically. Besides, we have also confirmed numerically that the smallest value of the data-misfit measure in the observed $m_t \times s$ curve occurs close to $s = 0$ in the case of noise-free data (Fig. 5a); in the case of noise-corrupted data, the minimum of s is displaced towards the positive s -axis (Fig. 5b). Finally, our new criterion for determining the true (or minimum) depth to the bottom of the source is theoretically sound. This criterion determines the true depth to the bottom of the source if the gravity anomaly has enough resolution to resolve it. A better resolution of the data is inferred from inspecting the existence of a well-defined minimum of s on the observed $m_t \times s$ curve, such as those produced by the shallow- and middle-bottomed dipping ducts (blue and red lines in Fig. 5). Otherwise, if the data

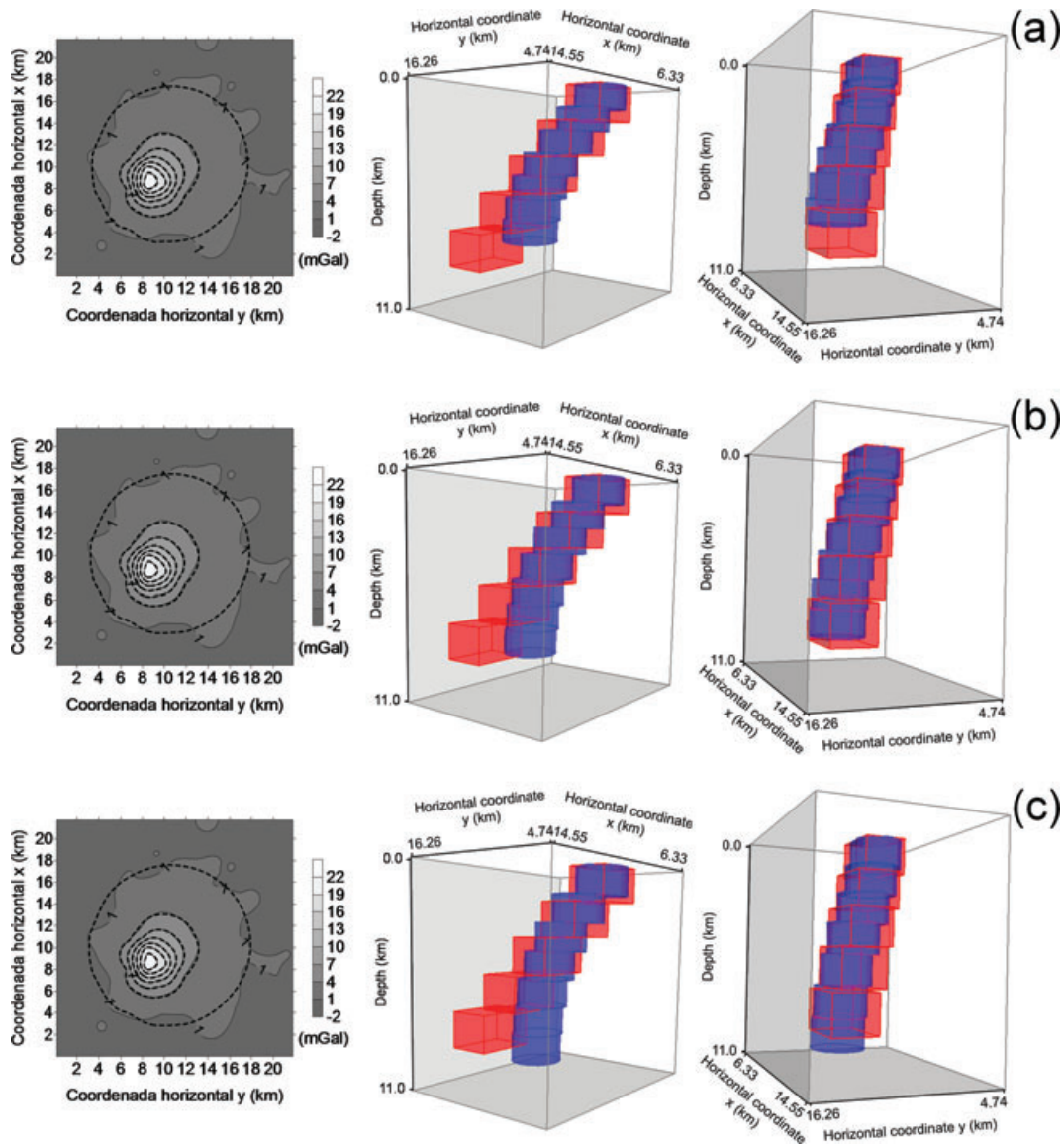


Figure 4. Synthetic data application produced by a simulated outcropping dipping duct. Perspective views of the true (red prisms) and estimated (blue prisms) deep-bottomed dipping duct; the latter is obtained by inverting the noise-corrupted gravity data (half-tone contour map) and assuming an interpretation model with maximum bottom depths z_{\max} (a) smaller (8 km); (b) equal (9 km) and (c) larger (10 km) than the true one. The corresponding fitted gravity anomalies produced by the estimated sources (blue prisms in a–c) are shown in dashed black lines in the contour maps (a)–(c).

do not have enough resolution, our criterion can determine, at most, the minimum depth to the bottom of the source and retrieve the geometry of part of the true source above this determined minimum depth. This aspect is illustrated in Fig. 4 whose shallowest part of the estimated geometries (blue prisms above the depth of 6 km) coincide with the upper portion of the true source (red prisms). A poor resolution of the data is evidenced by an observed $m_t \times s$ curve exhibiting an ill-defined minimum value of s , such as the one shown by the green line in Fig. 5(b).

4. APPLICATION TO SYNTHETIC DATA

We present two applications using synthetic gravity data simulating two different isolated geological sources with known density contrasts. In the first one we simulated an outcropping granitic pluton emplaced in homogeneous country rocks. In the second application

we simulated an outcropping dipping intrusive body having variable dips and strikes and exhibiting a complex form.

In all applications the irregularly distributed gravity data were computed on plane $z = 0$ km and contaminated with different pseudorandom Gaussian noise sequences with zero mean and a standard deviation as specified below. In each application we adopted the same practical procedure described in the Section 3.3 to obtain not only a stable solution that fits the data, but also to determine the true (or minimum) depth to the bottom of the source.

In all inversions, we set $z_0 = 0$ km because we simulated outcropping bodies and assumed that the depths to the tops of the interpretation models coincide with the actual tops of the sources. We established that all prisms defining the interpretation model have the same density contrast and the same number of the vertices of the polygons which describe their horizontal cross-sections. We also assumed the correct density contrast between the source and the host rocks.

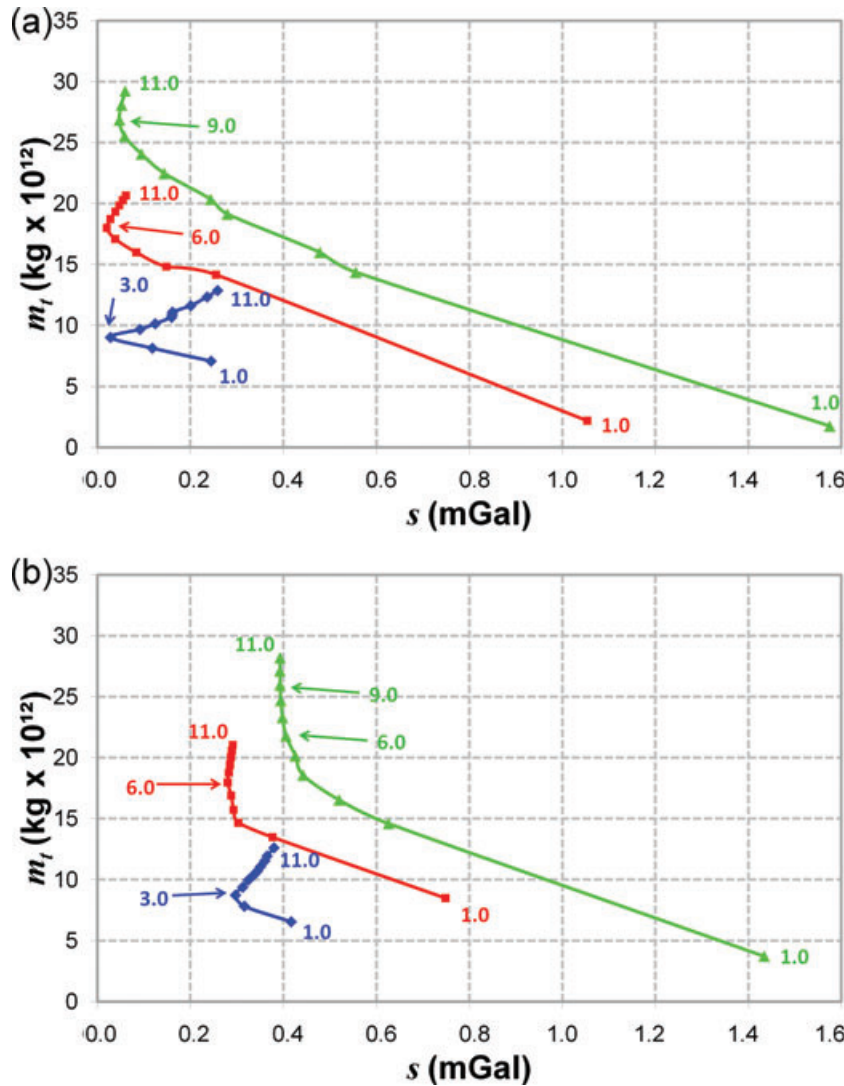


Figure 5. Observed $m_t \times s$ curves obtained for a simulated outcropping dipping volcanic ducts for noise-free (a) and noise-corrupted (b) data. The dots are associated with different values of maximum depths z_{max} assumed for the interpretation models. The blue, red and green lines are the observed $m_t \times s$ curves associated, respectively, with the shallow- (shown in Fig. 3), middle- (not shown) and deep- (shown in Fig 4) bottomed dipping ducts and whose depths to the bottom are 3, 6 and 9 km, respectively. The well-defined minimum of the data-misfit measure s yields an optimum estimate of the true depth to the bottom of the shallow- and middle-bottomed dipping ducts which are, respectively, 3 km (blue lines in a and b) and 6 km (red lines in a and b). The ill-defined minimum of the data-misfit measure s (green line in b) may determine, at most, a minimum depth to the bottom of the source.

In each application, we generated the observed $m_t \times s$ curve by computing seven estimates of m_t and s , each one associated with a fixed maximum depth z_{max} of the interpretation model in which the value of z_{max} varies from 3 km to 9 km in steps of 1 km leading to an uncertainty of ± 0.5 km.

4.1 Outcropping granite pluton

Fig. 6(a) shows the perspective view of a simulated outcropping granite pluton (grey prisms) with a constant density contrast of -0.09 g cm^{-3} relative to the homogeneous background. To simulate this granite pluton we set an ensemble of $L = 10$ prisms, with thicknesses $dz = 0.65$ km and with horizontal cross-sections described by polygons with $M^k = 30$ vertices, for all $k, k = 1, \dots, L$. By adopting the practical procedure described in the Section 2.3, we generated 30 pseudo-random sequences of random variables following a zero-mean Gaussian distribution with standard deviation

of 0.5 mGal, and added each noise sequence to the theoretical gravity anomaly (not shown) computed at 110 stations. This procedure created 30 sets of noise-corrupted gravity anomalies and Fig. 6(b) shows one of them (half-tone map) which differ from the other anomalies by small and random perturbations in the observations.

We inverted each noise-corrupted gravity anomaly using the proposed method to construct the observed $m_t \times s$ curve. In all inversions, we started with the same initial guess which consists of an ensemble of 10 vertically stacked prisms (dark grey prisms in Fig. 6a) compounding a vertical prism with polygonal cross-section inscribed into a cylindrical body with radius of 2 km whose horizontal Cartesian coordinates of the arbitrary origin are $xo^k = 9101.13$ km and $yo^k = 604.03$ km, for all $k, k = 1, \dots, L$. All constraints described in Section 2 have been used except for the fourth constraint (named the source's horizontal location constraint, see eq. 9d). We used $\mu = 1.0$, $\alpha_1 = 0.003$, $\alpha_2 = 0.0005$, $\alpha_3 = 0.5$, $\alpha_4 = 0.0$, $\alpha_5 = 0.3$ and $\alpha_6 = 0.00007$. In the case of the source's outcrop constraint (eq. 9c), the priorly specified radii ($r_j^o, j = 1, \dots, 30$) which

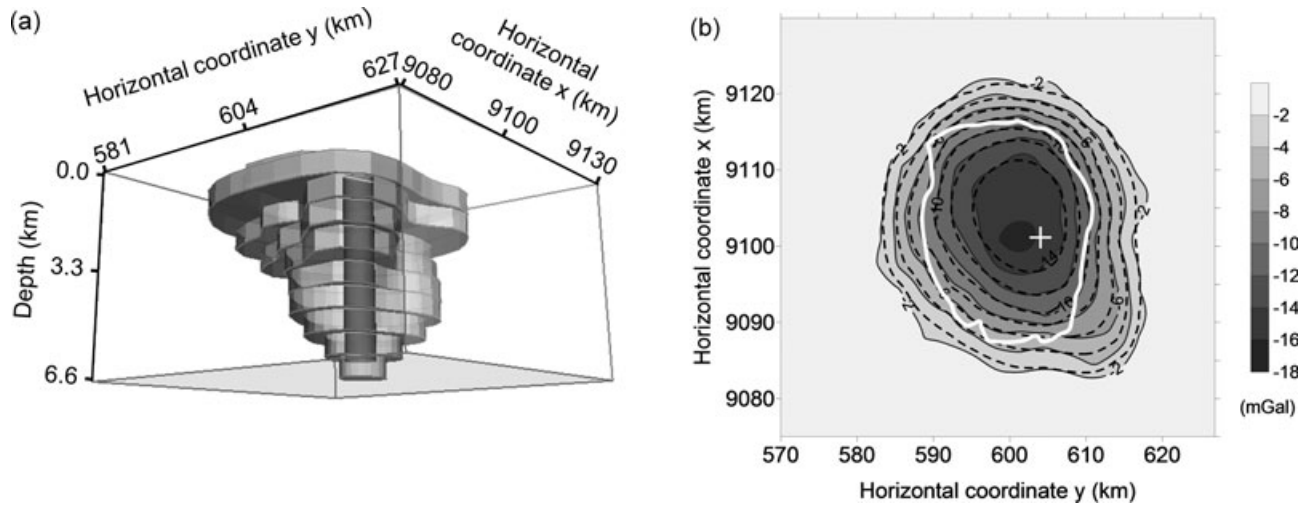


Figure 6. Synthetic data application produced by a simulated outcropping granite. (a) Perspective views of the simulated outcropping granite (light grey prisms) and the initial guess (dark grey prisms) used in all inversions. (b) Noise-corrupted gravity anomaly (half-tone contour map) produced by the granite shown in (a) and fitted gravity anomaly (dashed black lines) produced by the solution shown in Figs 7(b) and (c) (blue prisms). The intersection between the horizontal erosion surface and the interface separating the granite from the host rock is shown by the white line. The white cross indicates the priorly specified horizontal Cartesian coordinates (x_0° , y_0°) used in eq. 9c.

describe the edge of the polygonal cross-section of the first vertical prism were defined by using the known outcropping interface separating the granite from the host rock (white line in Fig. 6b). This set of priorly specified radii of the shallowest prism of the interpretation model will be referred to an origin whose priorly specified horizontal Cartesian coordinates are $x_0^\circ = 9101.13$ km and $y_0^\circ = 604.03$ km (white cross in Fig. 6b). We used $x_{\min} = 9090.0$ km, $x_{\max} = 9115.0$ km, $y_{\min} = 590$ km, $y_{\max} = 610$ km, $r_{\min} = 0$ km and $r_{\max} = 25$ km for all prisms. In the inversions, the interpretation model consists of an ensemble of $L = 10$ prisms with horizontal cross-sections described by polygons with $M^k = 30$ vertices, for all k , $k = 1, \dots, L$. Then, the 30 estimates are used to compute the stable sample mean parameter vector $\hat{\mathbf{m}}$ (eq. 10) that will be used to build the $m_i \times s$ curve.

Fig. 7(a) shows the observed $m_i \times s$ curve where the dots correspond to different values of maximum depths z_{\max} assumed for the interpretation models. We clearly note a well-defined minimum of s on the observed $m_i \times s$ curve, associated with $z_{\max} = 6$ km. Because this minimum is well defined, we conclude that the gravity data have good resolution to estimate the depth to the bottom of the simulated granite as 6 ± 0.5 km. Figs 7(b) and (c) show the perspective views of the estimated (blue prisms) and the true (red prisms) granites using the maximum depth $z_{\max} = 6$ km. Fig. 7(d) shows a set of horizontal depth slices of the estimated (blue lines) and true (red lines) upper edges of the polygonal cross-sections describing the geometry of the granite. This inversion result shows that the estimated 3-D body efficiently retrieves the true geometry of the granite body. The corresponding fitted anomaly is displayed in Fig. 6(b) in dashed black lines.

4.2 Outcropping dipping intrusion

We simulated an isolated outcropping dipping intrusion that is embedded in homogeneous rocks with a constant density contrast of 0.4 g cm^{-3} relative to the host rocks. This body fills a simulated opening created along a curved fracture. Fig. 8(a) displays a perspective view of this dipping intrusion (light grey prisms) whose shape resembles a spiral staircase. To simulate this intrusion we set

up an ensemble of $L = 14$ prisms, with thicknesses $dz = 0.5$ km and horizontal cross-sections described by polygons with $M^k = 16$ vertices, for all k , $k = 1, \dots, L$. Here, we adopted the same procedure described in the previous application. Hence, we inverted 30 sets of noise-corrupted gravity data obtained by adding different pseudo-random sequences of Gaussian noise, with zero mean and a standard deviation of 0.8 mGal, to the theoretical data. Fig. 8(b) shows one of them (half-tone map). To determine the bottom of the source and invert the gravity anomaly aiming at estimating the 3-D geometry of the simulated intrusion, we constructed initially the $m_i \times s$ curve (Section 3.3). In this way, we inverted the 30 sets of noise-corrupted gravity data by starting at the same initial guess shown in Fig. 8(a) by dark grey prisms. This initial guess has been selected on the basis of the anomaly features and it consists of two parts. In both parts, an ensemble of seven vertically stacked prisms compounding a vertical prism with polygonal cross-section inscribed into a cylindrical body with radius of 5 km. The first part is composed by the seven shallowest prisms that make up the interpretation model. All these prisms have the same horizontal Cartesian coordinates of the arbitrary origin, equal to $x_0^k = 51.671$ km and $y_0^k = 96.453$ km, $k = 1, \dots, 7$ (indicated by point A in Fig. 8b). The second part of the initial guess is composed by the seven deepest prisms that make up the interpretation model. All these prisms have the same horizontal Cartesian coordinates of the arbitrary origin of $x_0^k = 128.156$ km and $y_0^k = 65.686$ km, $k = 1, \dots, 7$, (indicated by point B in Fig. 8b). The horizontal Cartesian coordinates of the arbitrary origin related with the shallow- and the deep-seated cylinders were taken from the horizontal coordinates of, respectively, the gravity high and the smooth gravity signal (Fig. 8b). In the previous synthetic example, we assumed the knowledge about the intersection of the erosion surface with the interface separating the intrusion source from the host rock. Here, we assumed just the knowledge about the horizontal coordinates of the centre outcropping intrusion (eq. 9d) and assigned: $x_0^\circ = 38.420$ km and $y_0^\circ = 98.121$ km (white cross in Fig. 8b). We used $\mu = 1.0$, $\alpha_1 = 0.0005$, $\alpha_2 = 0.005$, $\alpha_3 = 0.0$, $\alpha_4 = 0.1$, $\alpha_5 = 0.1$ and $\alpha_6 = 0.00005$. Hence, all constraints described in Section 2 have been used, except for the third constraint (named the source's outcrop constraint presented in eq. 9c). We used $x_{\min} = 20$ km, $x_{\max} = 160$ km, $y_{\min} = 10$ km, $y_{\max} = 130$ km, $r_{\min} = 0$ km

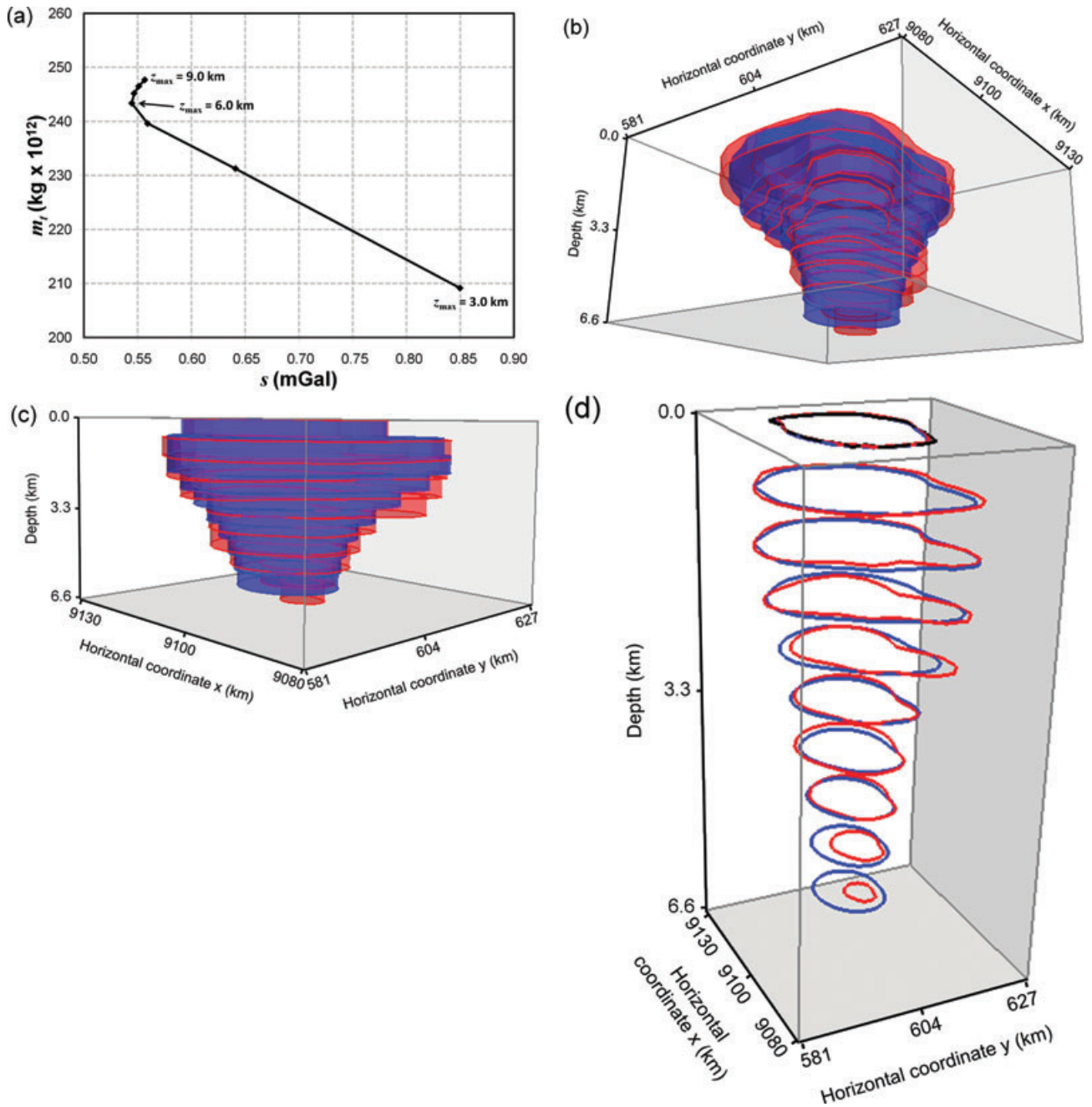


Figure 7. Synthetic data application produced by a simulated outcropping granite. (a) Observed $m_t \times s$ curve where the dots are associated with different values of maximum depths z_{max} assumed for the interpretation models. The well-defined minimum value of s , which is associated with $z_{\text{max}} = 6$ km, determines the depth to the bottom of the simulated granite. (b) and (c) Perspective views of the true (red prisms) and estimated (blue prisms) granites; the latter is obtained by inverting the gravity anomaly shown in Fig. 6(b) in half-tone contours and assuming an interpretation model with maximum bottom depth of 6.0 km estimated from the $m_t \times s$ curve criterion shown in (a). (d) Ensemble of horizontal depth slices of the true (red lines) and estimated (blue lines) edges of the polygonal cross-sections describing the geometry of the granite.

and $r_{\text{max}} = 50$ km for all prisms. In the inversions, the interpretation model consists of an ensemble of $L = 14$ prisms with horizontal cross-sections described by polygons with $M^k = 16$ vertices, for all k , $k = 1, \dots, L$.

Fig. 9(a) shows the observed $m_t \times s$ curve where the dots are related with the different maximum depths z_{max} assumed for the interpretation models. Again, the observed $m_t \times s$ curve reveals a well-defined minimum value of s , associated with $z_{\text{max}} = 7$ km, and provides a well-resolved depth-to-bottom estimate of 7 ± 0.5 km

for the simulated outcropping dipping intrusion, coinciding with the true depth to the bottom of this intrusion. Figs 9(b) and (c) show the perspective views of the estimated (blue prisms) and the true (red prisms) dipping intrusions using the maximum depth of $z_{\text{max}} = 7$ km for the interpretation model. Fig. 9(d) shows a set of horizontal depth slices of the estimated (blue lines) and true (red lines) upper edges of the polygonal cross-sections describing the geometry of the dipping intrusion. This solution shows the excellent performance of our method in recovering the 3-D geometry of true

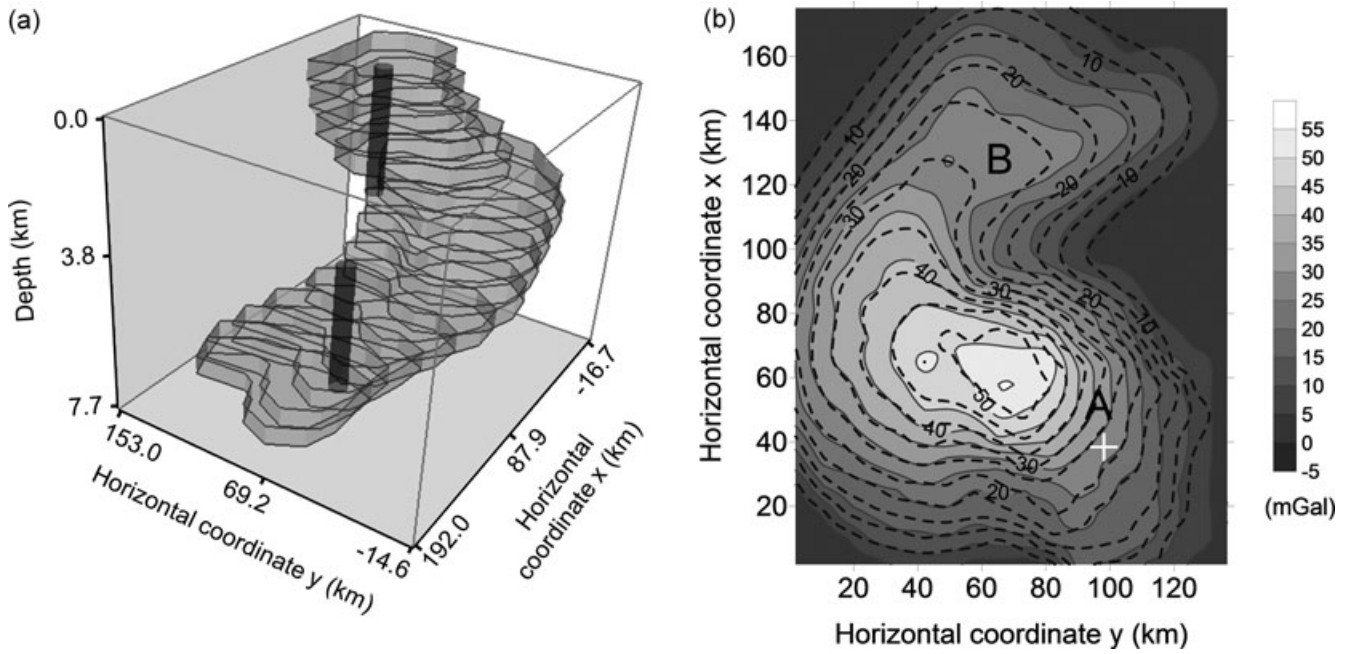


Figure 8. Synthetic data application produced by a simulated outcropping dipping intrusion. (a) Perspective views of the simulated dipping intrusion (light grey prisms) and the initial guess (dark grey prisms) used in all inversions. (b) Noise-corrupted gravity anomaly (half-tone contour map) produced by the intrusion shown in (a) and fitted gravity anomaly (dashed black lines) produced by the solution shown in Figs 9(b) and (c) (blue prisms). The white cross indicates the priorly specified horizontal Cartesian coordinates (x_o^o , y_o^o) used in eq. 9d. Points A and B define the horizontal coordinates where the two parts of the initial guess are located.

dipping intrusion resembling a spiral staircase-shaped feature. The corresponding fitted anomaly is shown in Fig. 8(b) in dashed black lines.

5. APPLICATION TO REAL DATA

The Archean Matsitama greenstone belt in northeastern Botswana occurs at the southwestern extremity of the Zimbabwe Craton (Ranganai *et al.* 2002; McCourt *et al.* 2004). Fig. 10 shows a simplified geological map of Matsitama, northeastern Botswana, where the greenstone belt from Matsitama becomes progressively masked to the west because of the overlying Kalahari and Karoo sediments. The original gravity observations (see Reeves 1985; Silva *et al.* 2007) indicates that greenstone rocks extend themselves westwards and then northeastwards (open circles in Fig. 10). In this area, a shallow borehole directed to coal exploration in the sedimentary cover confirmed the presence of Precambrian ultramafic rocks.

Fig. 11 shows the residual Bouguer anomaly map (half-tone map) over the Matsitama greenstone belt. We used the same practical procedure described for the previous test. Hence, we produced and inverted 30 sets of noise-corrupted gravity anomalies obtained by adding different pseudorandom sequences of Gaussian noise, with zero mean and a standard deviation of 0.8 mGal, to the field data (half-tone map in Fig. 11). We stress that the only physical aim of adding extra noise to field data is to analyse the solution stability. The final estimates are obtained with the original observations in all inversions we have started at the same initial guess and have assumed the constant density contrast of 0.4 g cm^{-3} between the Matsitama intrusion and the country rocks. We also set an interpretation model with $L = 14$ prisms, with a constant density contrast of 0.4 g cm^{-3} and with horizontal cross-sections described by polygons with $M^k = 16$ vertices, for all k , $k = 1, \dots, L$. Then,

the 30 estimates are used to compute the stable sample mean parameter vector $\hat{\mathbf{m}}$ (eq. 10) that has been used to build the $m_i \times s$ curve.

Based on the synthetic application to interpret an outcropping dipping intrusion, shown in Section 4.2, the initial guess (not shown) consists of two ensembles of seven vertically stacked prisms, each one consisting of a vertical prism with polygonal cross-section, inscribed into a cylindrical body with radius 5 km and with different horizontal coordinates of the centre. The first ensemble is composed of the seven shallowest prisms that make up the interpretation model with horizontal Cartesian coordinates of the arbitrary origin equal to $x_o^k = 51.671 \text{ km}$ and $y_o^k = 96.453 \text{ km}$, $k = 1, \dots, 7$. These horizontal Cartesian coordinates (point A in Fig. 11) were chosen as the horizontal coordinates close to the gravity high. The second ensemble is composed of the seven deepest prisms that make up the interpretation model with horizontal Cartesian coordinates of the arbitrary origin equal to $x_o^k = 128.16 \text{ km}$ and $y_o^k = 65.69 \text{ km}$. These horizontal Cartesian coordinates were chosen as those located at the smooth gravity signal (point B in Fig. 11). The Matsitama intrusion is in fact a shallow buried body; however, here we assumed that this body crops out and that the knowledge about the horizontal coordinates of its shallowest portion is $x_o^o = 38.420 \text{ km}$ and $y_o^o = 98.121 \text{ km}$ (white cross in Fig. 11). Hence, all constraints described in the Section 2 have been used except for the third constraint (named the source's outcrop constraint; see eq. 9c) because the shallowest boundary of the intrusion is unknown. The inversion control variables used in all inversions are $\mu = 1.0$, $\alpha_1 = 0.0001$, $\alpha_2 = 0.001$, $\alpha_3 = 0.0$, $\alpha_4 = 0.1$, $\alpha_5 = 0.01$ and $\alpha_6 = 0.00005$. We used $x_{o\min} = 20 \text{ km}$, $x_{o\max} = 160 \text{ km}$, $y_{o\min} = 10 \text{ km}$, $y_{o\max} = 130 \text{ km}$, $r_{\min} = 0 \text{ km}$ and $r_{\max} = 50 \text{ km}$ for all prisms.

According to the criterion described in the Section 3.3 the minimum of s on the observed $m_i \times s$ curve is associated with the true

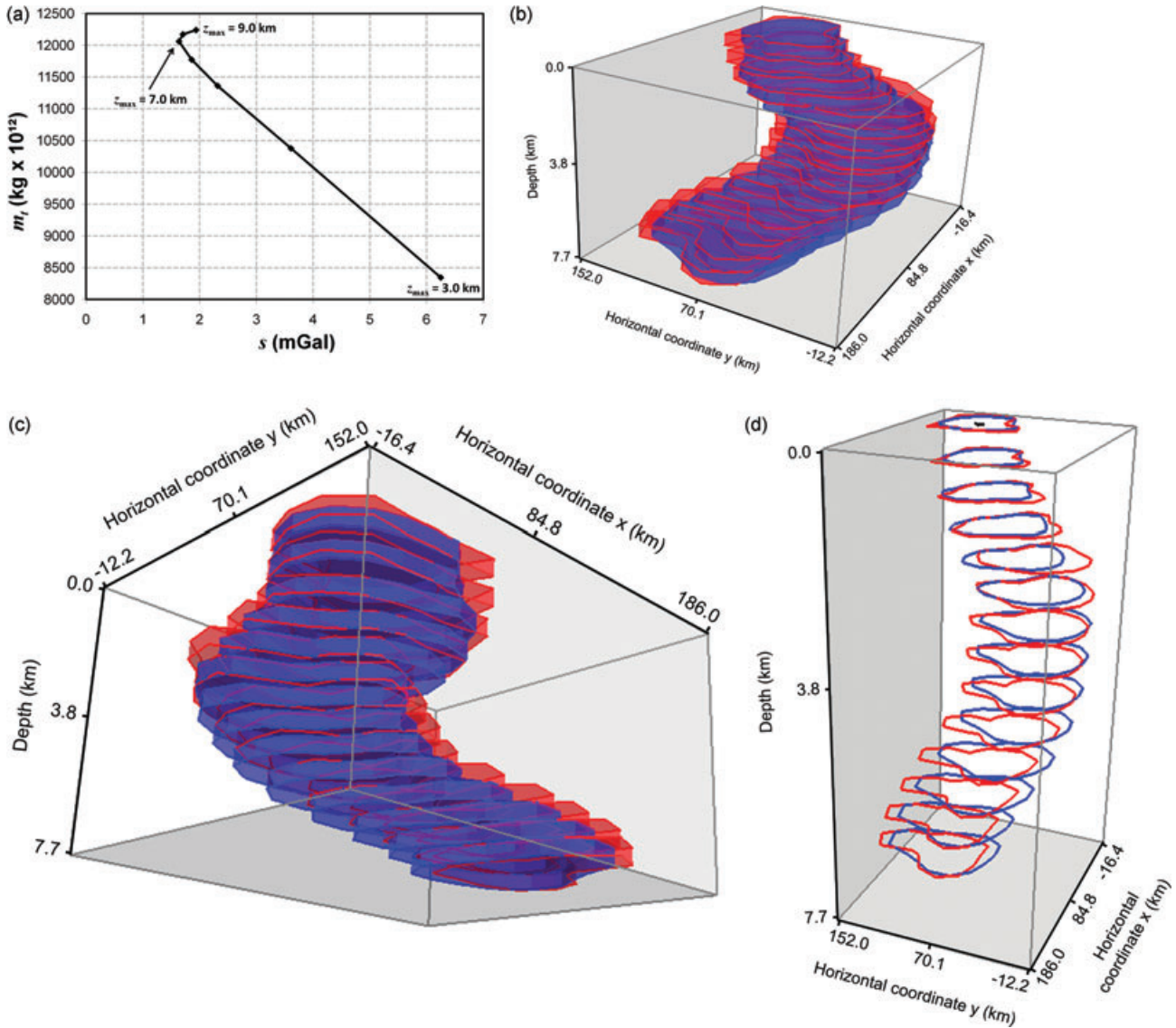


Figure 9. Synthetic data application produced by a simulated outcropping dipping intrusion. (a) Observed $m_t \times s$ curve where the dots are associated with different values of maximum depths z_{max} assumed for the interpretation models. The well-defined minimum value of s , which is associated with $z_{\text{max}} = 7 \text{ km}$, determines the depth to the bottom of the simulated intrusion. (b) and (c) Perspective views of the true (red prisms) and estimated (blue prisms) intrusions; the latter is obtained by inverting the gravity anomaly shown in Fig. 8(b) in half-tone contours and assuming an interpretation model with maximum bottom depth of 7 km estimated from the $m_t \times s$ curve criterion shown in (a). (d) Ensemble of horizontal depth slices of the true (red lines) and estimated (blue lines) edges of the polygonal cross-sections describing the geometry of the dipping intrusion.

(or minimum) depth of the source, depending on whether the true source produces a gravity anomaly that is able (or not) to resolve the source's bottom. We generated the observed $m_t \times s$ curve by computing eight estimated values of m_t and s , each one associated with a fixed maximum depth z_{max} of the interpretation model, in which the value of z_{max} varies from 3 km to 10 km in steps of 1 km leading to an uncertainty of $\pm 0.5 \text{ km}$. Fig. 12(a) shows that the minimum of s is associated with a depth to the bottom of $8.0 \pm 0.5 \text{ km}$. Because this $m_t \times s$ curve shows a well-defined minimum of s , it suggests that the gravity data are able to resolve the depth-to-bottom estimate of the Matsitama intrusion. The estimated source fits acceptably the gravity anomaly (dashed black lines in Fig. 11) and retrieves a dipping intrusion with variable dips and strikes with bottom's depth of $8 \pm 0.5 \text{ km}$ (Figs 12b and c). This result is consistent with the available geological information reported by Reeves (1985) that

the greenstone rocks extend themselves westwards. However, the anomaly fit obtained in the Matsitama application (dashed black lines in Figs 12b and c) is worse than that obtained in the synthetic applications. This poorer fitting yielded in Matsitama application may be related to possible violations of premises assumed by our method. The presence of multiple sources, for example, giving rise to an interfering gravity anomaly, may produce a poor data fit. Another possibility is that we inverted a truncated gravity anomaly (half-tone map in Fig. 11).

6. CONCLUSIONS

We have proposed a gravity-inversion method and the $m_t \times s$ curve criterion to estimate the 3-D geometry of isolated sources,

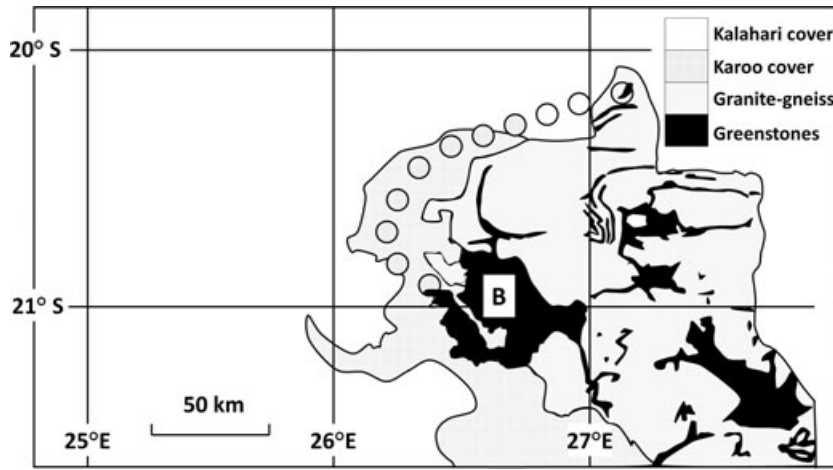


Figure 10. Simplified geological map of Matsitama, northeastern Botswana, displaying igneous rocks (B) and its extension (open circles), inferred by the inspection of the original Bouguer anomaly map (not shown). After Reeves (1985).

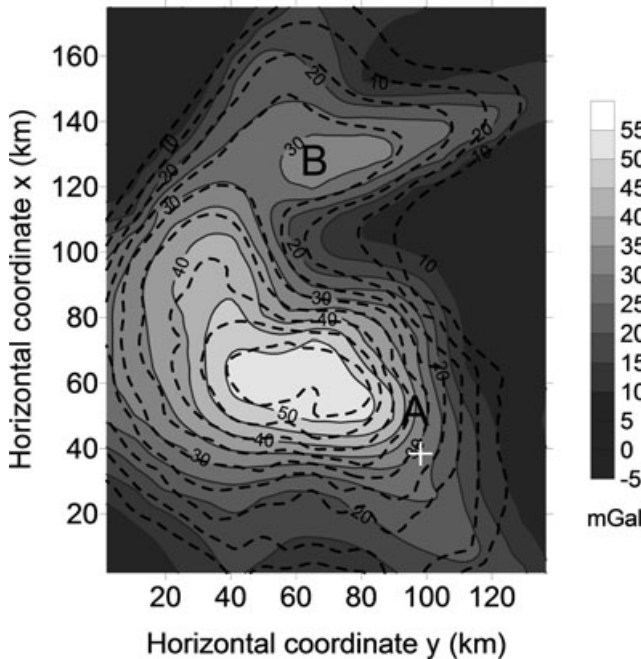


Figure 11. Matsitama greenstone rocks (Botswana). Bouguer anomaly map (half-tone contour map) from the Matsitama area corrected for gravity effects produced by the Moho. The dashed black lines show the fitted Bouguer anomaly produced by the corresponding estimated source in Fig. 12(b) and (c). The white cross indicates the prior specified horizontal Cartesian coordinates (x_0° , y_0°) used in eq. 9d. Points A and B define the horizontal coordinates where the two parts of the initial guess are located.

assuming the knowledge about the density contrast and about the depth to the source's top. Our method implicitly introduces homogeneity and compactness constraints through the interpretation model which consists of a set of 3-D vertical, juxtaposed prisms in the vertical direction, whose thicknesses and density contrasts are known and whose horizontal cross-sections are described by an arbitrary and unknown polygon. The geometry of the 3-D source is defined by estimating the geometry of the set of polygons defining the horizontal sections of vertically stacked prisms. The polygon vertices of each prism are described by polar coordinates with an

unknown origin inside the top of the prism. Our method estimates the radii associated with polygon vertices for a fixed number of equally spaced angles spanning the interval between 0° and 360° , and the horizontal Cartesian coordinates of the arbitrary origin. To guarantee a stable solution which fits the gravity data, our method imposes constraints on the source shape. Although the estimated source shape is stable and yields an acceptable anomaly fit, it depends on the maximum depth assumed by the interpretation model.

We have proposed a new criterion to reduce the class of possible solutions compatible with the gravity anomaly and to determine the optimum depth-to-bottom estimate of the source. This criterion is based on the estimated data-misfit measure (s) and on the estimated total-anomalous mass (m_t). These estimates are computed along successive inversions by using different tentative maximum depths for the interpretation model. The tentative value for the maximum depth producing the smallest data-misfit measure is the best estimate of the bottom's depth of the source and it is chosen by means of a $m_t \times s$ curve for the range of different tentative maximum depths. This criterion was extensively tested with synthetic data. In the case that a minimum of s on the $m_t \times s$ curve is well defined, the method always produced correct estimates of the bottom's depth of the source and recovered the 3-D geometry of the source. Conversely, if the smallest value of s on the $m_t \times s$ curve is ill-defined, the $m_t \times s$ curve criterion may only determine a minimum source's depth to the bottom. Even in this case, our inversion method retrieves the upper portion of the source above the lower bound estimated for the source's depth to the bottom.

This inversion method and the $m_t \times s$ curve criterion have been applied to both synthetic and field data sets showing their efficiency in retrieving the geometry of 3-D sources, even in the case of a complex simulated body with variable dips and strikes that intrudes a curved fracture, a unique characteristic among most 3-D gravity-inversion methods. This inversion method has the advantage of requiring no explicit assumption about the geometry of the anomalous source and, because the interpretation model consists of homogeneous prisms, no constraints favouring homogeneity and compactness are required, which makes it operationally simple. However, the method is restricted to isolated sources with known depth to the top and density contrast. When these assumptions hold and the gravity data have sufficient resolution, the inversion method and the $m_t \times s$ curve criterion produce good estimates of the geometry of the anomalous source. Otherwise, the estimated solution may

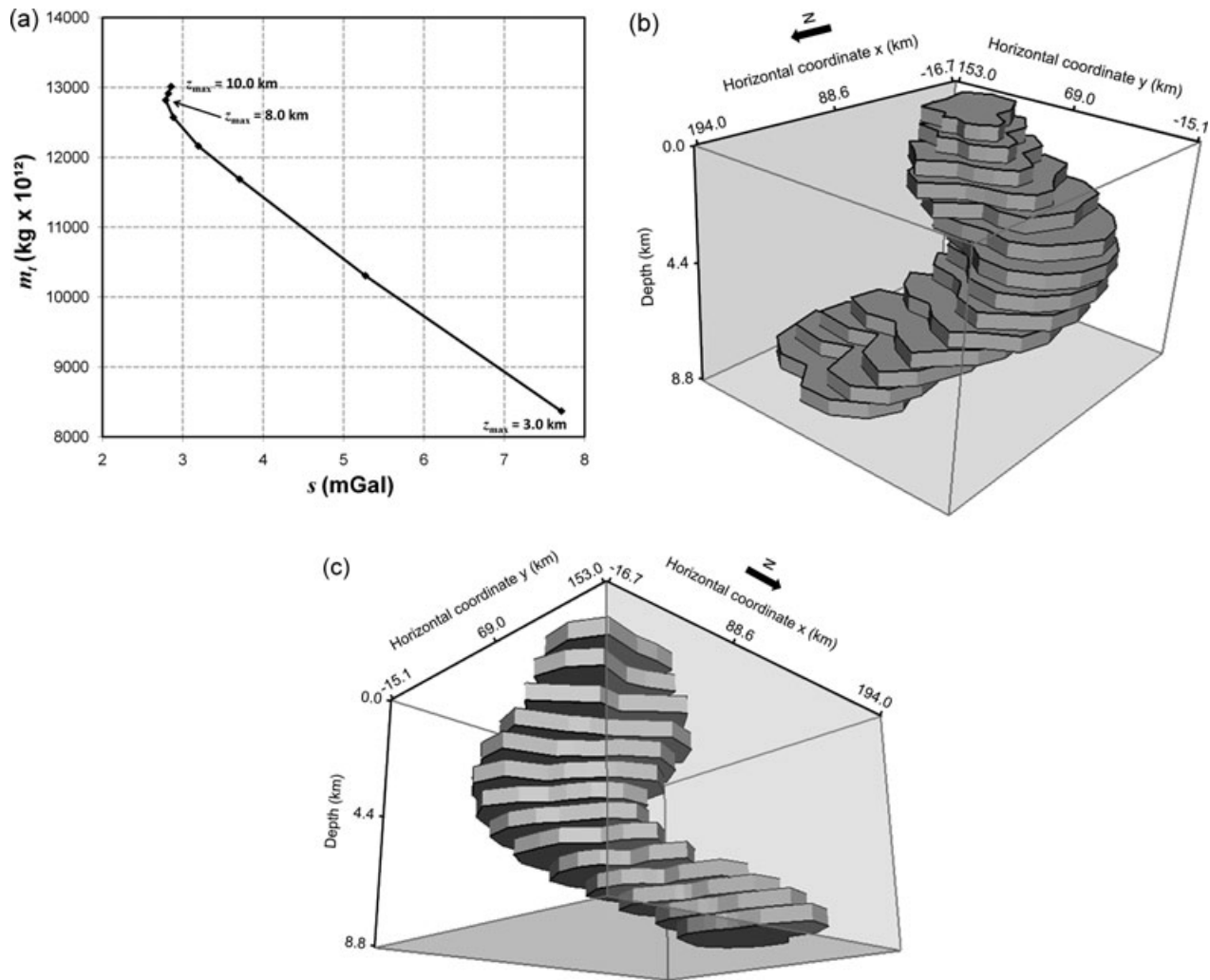


Figure 12. Matsitama greenstone rocks (Botswana). (a) Observed $m_t \times s$ curve where the dots are associated with different values of maximum depths z_{\max} assumed for the interpretation models. The well-defined minimum value of s , which is associated with $z_{\max} = 8$ km, determines the depth to the bottom of the Matsitama intrusion. (b) and (c) Perspective views of the initial guess (dark grey prisms) used in all inversions and the estimated 3-D geometry of the greenstone belt (light grey prisms) obtained by inverting the gravity anomaly shown in Fig. 11 in half-tone contours.

produce a poor anomaly fit and may fail to retrieve the geometry of the gravity source.

Our method can be extended to invert interfering gravity anomalies produced by multiple sources. Additionally, the 3-D radial inversion can be extended to invert magnetic data and the gradient components of gravity and magnetic data.

ACKNOWLEDGMENTS

We thank an anonymous editor and two reviewers Horst Holstein and Fabio Caratori Tontini for their valuable criticism. The authors were supported in this research by fellowships (VCF and JBCS) from Conselho Nacional de Desenvolvimento Científico e Tecnológico (CNPq) and scholarship (VCO Jr) from Coordenação de Aperfeiçoamento de Pessoal de Nível Superior (CAPES), Brazil.

REFERENCES

- Barbosa, V.C.F. & Silva, J.B.C., 1994. Generalized compact gravity inversion, *Geophysics*, **59**, 57–68.
- Barbosa, V.C.F. & Silva, J.B.C., 2006. Interactive 2D magnetic inversion: a tool for aiding forward modeling and testing geologic hypotheses, *Geophysics*, **71**, L43–L50.
- Barbosa, V.C.F., Silva, J.B.C. & Medeiros, W.E., 1999a. Stable inversion of gravity anomalies of sedimentary basins with nonsmooth basement reliefs and arbitrary density contrast variations, *Geophysics*, **64**, 754–764.
- Barbosa, V.C.F., Silva, J.B.C. & Medeiros, W.E., 1999b. Gravity inversion of a discontinuous relief stabilized by weighted smoothness constraints on depth, *Geophysics*, **64**, 1429–1437.
- Barbosa, V.C.F., Silva, J.B.C. & Medeiros, W.E., 2002. Practical applications of uniqueness theorems in gravimetry, part II: pragmatic incorporation of concrete geologic information, *Geophysics*, **67**, 795–800.
- Bertete-Aguirre, H., Cherkaev, E. & Oristaglio, M., 2002. Non-smooth gravity problem with total variation penalization functional, *Geophys. J. Int.*, **149**, 499–507.
- Blakely, R.J., 1995. *Potential Theory in Gravity and Magnetic Applications*, Cambridge University Press, Cambridge.
- Calcagno, P., Chilès, J.P., Courrioux, G. & Guillen, A., 2008. Geological modelling from field data and geological knowledge, part I. Modelling method coupling 3D potential-field interpolation and geological rules, *Phys. Earth planet. Inter.*, **171**, 147–157.

- Guillen, A. & Menichetti, V., 1984. Gravity and magnetic inversion with minimization of a specific functional, *Geophysics*, **49**, 1354–1360.
- Hammer, S., 1945. Estimating ore masses in gravity prospecting, *Geophysics*, **10**, 50–62.
- LaFehr, T.R., 1965. The estimation of the total amount of anomalous mass by Gauss's theorem, *J. geophys. Res.*, **70**, 1911–1919.
- Last, B.J. & Kubik, K., 1983. Compact gravity inversion, *Geophysics*, **48**, 713–721.
- Luo, X., 2010. Constraining the shape of a gravity anomalous body using reversible jump Markov chain Monte Carlo, *Geophys. J. Int.*, **180**, 1067–1089.
- Marquardt, D.W., 1963. An algorithm for least-squares estimation of non-linear parameters, *J. Soc. Ind. appl. Math.*, **2**, 601–612.
- McCourt, S., Kampunzu, A.B., Bagai, Z. & Armstrong, R.A., 2004. The crustal architecture of Archaean terranes in Northeastern Botswana, *S. Afr. J. Geol.*, **107**, 147–158.
- Moraes, R.A.V. & Hansen, R.O., 2001. Constrained inversion of gravity fields for complex 3D structures, *Geophysics*, **66**, 501–510.
- Plouff, D., 1976. Gravity and magnetic fields of polygonal prisms and application to magnetic terrain corrections, *Geophysics*, **41**, 727–741.
- Portniaguine, O. & M.S. Zhdanov, 1999. Focusing geophysical inversion images, *Geophysics*, **64**, 874–887.
- Ranganai, R.T., Kampunzu, A.B., Atekwana, E.A., Paya, B.K., King, J.G., Koosimile, D.I. & Stettler, E.H., 2002. Gravity evidence for a larger Limpopo belt in southern Africa and geodynamic implications. *Geophys. J. Int.*, **149**, F9–F14.
- Reeves, C.V., 1985. The Kalahari Desert, central southern Africa: a case history of regional gravity and magnetic exploration, in, *The Utility of Regional Gravity and Magnetic Anomaly Maps*, pp. 144–153, ed. Hinze, W.J., SEG.
- Silva, J.B.C. & Barbosa, V.C.F., 2004. Generalized radial inversion of 2D potential field data, *Geophysics*, **69**, 1405–1413.
- Silva, J.B.C. & Barbosa, V.C.F., 2006. Interactive gravity inversion, *Geophysics*, **71**, J1–J9.
- Silva, J.B.C., Medeiros, W.E. & Barbosa, V.C.F., 2001a. Potential field inversion: choosing the appropriate technique to solve a geologic problem, *Geophysics*, **66**, 511–520.
- Silva, J.B.C., Medeiros, W.E. & Barbosa, V.C.F., 2001b. Pitfalls in nonlinear inversion, *Pure appl. Geophys.*, **158**, 945–964.
- Silva, J.B.C., Oliveira, F.S., Barbosa, V.C.F. & Campos Velho, H.F., 2007. Apparent-density mapping using entropic regularization, *Geophysics*, **72**, I51–I60.
- Silva Dias, F.J.S., Barbosa, V.C.F. & Silva, J.B.C., 2009. 3D gravity inversion through an adaptive learning procedure, *Geophysics*, **74**, I9–I21.
- Tikhonov, A.N. & Arsenin, V.Y., 1977. *Solutions of Ill-Posed Problems*, W. H. Winston & Sons, Washington, DC.
- Wildman R.A. & Gazonas, G.A., 2009. Gravitational and magnetic anomaly inversion using a tree-based geometry representation, *Geophysics*, **74**, I23–I35.